

CFD Validation Using Data From A Classic Experimental Test Program for a Highly Contoured Body of Revolution Having Regions of Convergent /Divergent Flows With Adverse/Favorable Pressure Gradients.

Brenda M. Kulfan¹,

Boeing Commercial Airplanes, Retired, Auburn, WA, 98092

An important element in the development of a CFD design or analysis tool involves the validation and / or calibration of the methodology using experimental and /or other computational data. The various types of validation processes include, full configuration studies, major component studies and when possible, fundamental flow physics studies. Fundamental flow physics type of experimental studies, have commanded less interest and consequently less funding in recent years. Consequently, locating, using and retaining data from unique and quality fundamental types of experiments should become increasingly more important.

The objectives of this presentation are threefold.

1. Introduce a classic and very unique fundamental flow physics type of wind tunnel test program.
2. Illustrate the use of extensive experimental data from the wind tunnel test program in a recent CFD validation study.
3. Encourage the retention and future usage of the test data for code validation studies.

The experimental model from this unique wind tunnel test program was a highly contoured body of revolution designed to have regions of converging and diverging flows, and both favorable and unfavorable pressure gradients. This report includes numerous comparisons of the experimental test data with theoretical predictions obtained with the TRANAIR nonlinear potential flow code with coupled boundary layer. The comparisons include distributions of Mach number, surface pressures, pressure drag, local skin friction, and viscous drag as well as integrated velocity profile parameters such as displacement thickness, momentum thickness and shape factor. The results presented in this report illustrate that in certain circumstances, comparisons of theoretical and experimental over all forces are not alone sufficient to assess the validity of a theoretical methodology. Any validation process should therefore include detailed fundamental comparisons such as those presented in this study.

I. Introduction

An important element in the development of a CFD design or analysis process involves the validation and / or calibration of the methodology using experimental and /or other computational data. The various types of validation processes include, full configuration studies, major component studies and when possible, fundamental flow physics studies. Fundamental flow physics type of experimental studies, have commanded less interest and consequently less funding in recent years. Consequently, locating, using and retaining data from unique and quality fundamental types of experiments should become increasingly more important.

The objectives of this presentation are threefold.

1. Introduce a classic and very unique fundamental flow physics type of wind tunnel test program.
2. Illustrate the use of extensive experimental data from the wind tunnel test program in a recent CFD validation study.
3. Encourage the retention and future usage of the test data for code validation studies.

¹ Retired Engineer/Scientist – Technical Fellow, 11055 SE 295th Street, Auburn WA, AIAA Member.

The objectives of this report are therefore similar to the code validation study discussed in references 1 and 2 that utilized a classic set of wind tunnel data from another unique wind tunnel test program. The wind tunnel test program^{3,4,5} discussed in this report was conducted in about 1965 to determine the influence of Mach number, favorable and adverse pressure gradients, and streamline convergence and divergence on the development of turbulent boundary layers. The model was a highly contoured body of revolution shown in figure 1 and discussed in section 2. The experimental measurements included pressure distributions, local skin friction distributions and boundary-layer profiles along the body, at Mach numbers between 0.6 and 2.8 and Reynolds numbers, based on the length of the body, between 5×10^6 and 2×10^7 . The study was a result of collaboration between the Aerodynamische Versuchsanstalt, Göttingen and the Royal Aircraft Establishment, Bedford. The experiments were conducted in the RAE 8ft x 8ft wind tunnel. In this report the model will be called the Winter-Smith-Rotta body or the WSR body.

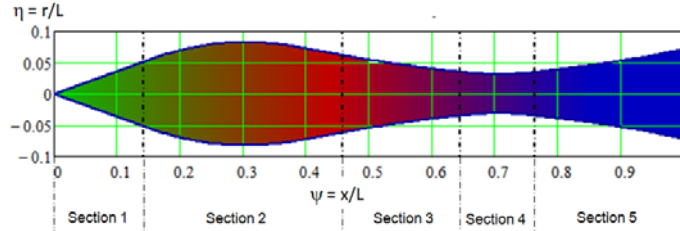


Figure 1: Winter Smith Rotta (WSR) Body

II. WSR Body Geometry

The primary objective of the original wind tunnel test program was to produce an axisymmetric converging flow with an adverse pressure gradient while at the same time providing information on the behavior of turbulent boundary layers on compressible flows with pressure gradients. Such data would be considered to be of great value in developing and checking methods of calculation.

An obvious simple example of a supersonic flow with an adverse pressure gradient and converging streamlines is the aft end of a parabolic body of revolution. Thus the starting point for the model design was a body approximating a parabolic body over the front of the model with concavity introduced over the aft end. A flare was added to the aft end of the body to obtain a diverging flow, while hopefully retaining some part an adverse pressure gradient. The selection of an axisymmetric body of revolution also avoided experimental difficulties of boundary-layer exploration associated with unknown crossflow conditions.

The final shape of the model as shown in Figure 1, was defined with five sections with continuity of ordinate, slope and curvature at the junctions of the sections except at the end of the conical part of the nose, (section 1), where the curvature is discontinuous.

The first section, $0.0 \leq \psi \leq (\psi_1 = 0.14158)$, was defined as a conical nose with an included angle of 40 degrees, which is the largest angle for an attached shock at the lowest supersonic speed of the test program (Mach = 1.4).

$$\eta(\psi) = 0.36397\psi \quad (1)$$

Where: $\psi = x/L$ and $\eta = r/L$

x is the body station

r is the body radius at station x

L is the body length

The second section, $0.14158 < \psi \leq (\psi_2 = 0.45725)$, was defined by a quartic curve which matched the conical nose of section 1 at station ψ_1 in ordinate and slope.

$$\eta(\psi) = 6.34730\psi^4 - 6.49221\psi^3 + 1.22668\psi^2 + 0.33498\psi - 0.00461 \quad (2)$$

The maximum radius occurs in this section at the station $\psi_{max} = 0.30$.

The third section, $0.45725 < \psi \leq (\psi_3 = 0.64473)$, was defined by a cubic equation that had approximately constant convergence.

$$\eta(\psi) = -0.236382\psi^3 + 0.607620\psi^2 - 0.595521\psi + 0.229694 \quad (3)$$

Geometric divergence and convergence are defined as:

Divergence: $\frac{1}{r(x)} \cdot dr/dx > 1$ (4)

Convergence: $\frac{1}{r(x)} \cdot dr/dx < 1$ (5)

The fourth section, $0.64473 < \psi \leq (\psi_4 = 0.76317)$, was defined by a quartic equation:
 $\eta(\psi) = -53.58258\psi^4 + 150.87806\psi^3 - 158.03866\psi^2 + 72.96859\psi - 12.4939$ (6)

The minimum radius occurs in this section at the station $\psi_{min} = 0.705$

The fifth section, $0.76317 < \psi \leq (\psi_5 = 1.0)$, defined the final flare of the body having approximately constant divergence and was a mirror image of the third section.

$\eta(\psi) = 0.236382\psi^3 - 0.390789\psi^2 + 0.290242\psi - 0.064001$ (7)

Figure 2 shows the slopes, curvature and divergence/convergence distributions of the WSR body.

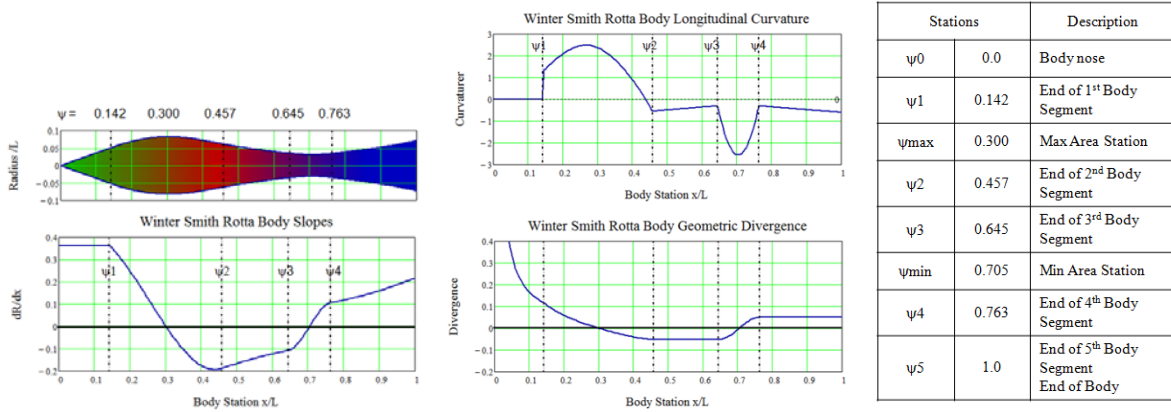


Figure 2: WSR Slopes, Curvature and Divergence/Convergence Distributions

As summarized in figures 3 and 4 the WSR body produced streamline divergence and convergence, and as will be shown later in this report, regions of both favorable and adverse pressure gradients.

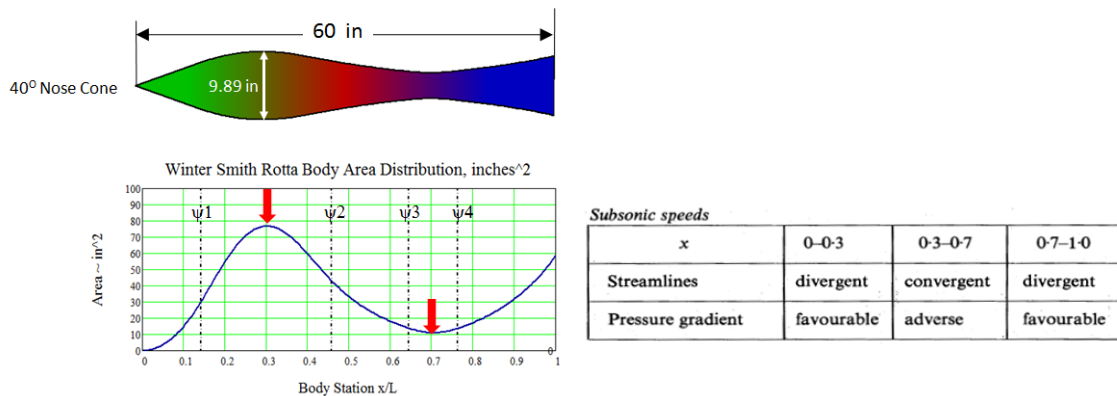
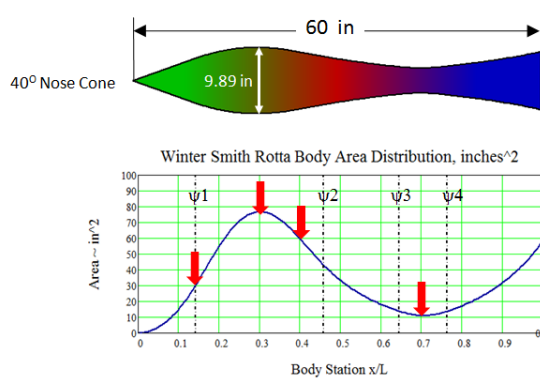


Figure 3: WSR Body Characteristics at Subsonic Speeds



Supersonic speeds

x	0-0.142	0.142-0.3	0.3-0.4	0.4-0.7	0.7-1.0
Streamlines	divergent	divergent	convergent	convergent	divergent
Pressure gradient	zero	favourable	favourable	adverse	slightly adverse

Figure 4: WSR Body Characteristics at Supersonic Speeds

III. WSR Wind Tunnel Test Program

The wind tunnel test program included skin friction and pressure measurements obtained along the length of the body, velocity profile measurements at a number of body stations and a number of schlieren pictures. The test conditions included a range of subsonic and supersonic Mach numbers and a number of Reynolds numbers.

The surface pressures were measured at 29 stations along the length of the body on top of the body defined as $\theta = 90$ degrees. The skin friction measurements were obtained along a similar row pressure ports at the 29 stations along the body at $\theta = 30$ degrees using the razor blade technique described in section 4. The test conditions for which the pressure and skin friction measurements were made are summarized in figure 5.

Skin Friction and Cp Distributions were measured at 29 stations along the body.

M_∞	0.6	0.8	1.4	1.7	2.0	2.4	2.8
10^{-6} Rel	10	10	5 10 20	10	5 10 17	10	5 10

C_f Accuracy $\approx \pm 0.0002$ at Rel $\sim 10^7$

Figure 5: Skin Friction and CP Measurement Test Conditions

Velocity profiles were also obtained at six body stations and at the flow conditions shown in figure 6. Reference 5 contains a detailed description of the velocity profile measurement instrumentation and techniques. Integrated boundary layer growth parameters including displacement thickness, δ^* , momentum thickness, θ , and the shape factor, H, were obtained for all of the measured velocity profiles.

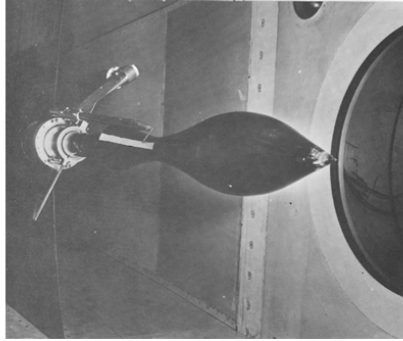
Velocity Profiles were measured at $x/L = 0.4, 0.475, 0.55, 0.7, 0.833, 0.983$

M_∞	0.6	1.4	1.7	2.0	2.4	2.8
10^{-6} Rel	10	10 20	10	10	10	10

Figure 6: Boundary Layer Measurements Test Conditions

Figure 7 shows pictures of the WSR body in the wind tunnel along with the boundary layer survey equipment.

Model with boundary-layer survey equipment



Detail of Model With Rake

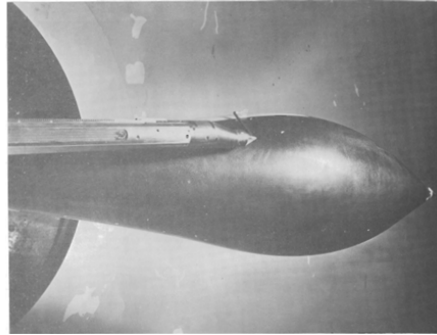


Figure 7: WSR Body in the Wind Tunnel

For all experiments a transition trip was attached 1.5 inches from the nose of the body corresponding to 2.5% Of the body length. A 0.005 inch Ballotini type trip was used. According to the authors of the test reports “*The size proved to be inadequate at Mach numbers above 1.4.*” However as will be shown later in this report it appears that the trips were effective for all test conditions except the lowest Reynolds number which were approximately 5×10^6 .

Figure 8 shows an example of the experimental velocity profile measurement data. The experimental velocity profile measurements were not used in the present study since the TRANAIR CFD program incorporates a momentum integral boundary layer method and consequently does not calculate specific velocity details within the boundary layer.

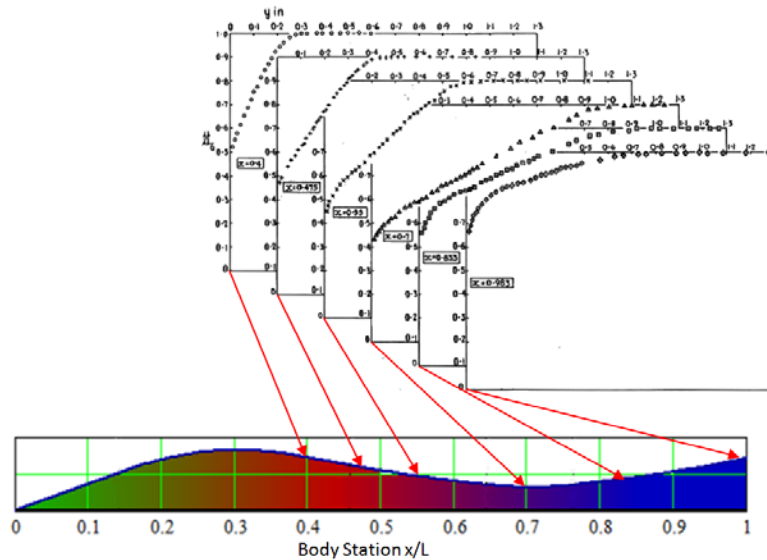


Figure 8: Experimental Velocity Profile Measurement Data, Mach = 0.597 $Re_l = 9.85 \cdot 10^6$ $x_t/c = 0.025$

IV. WSR Indirect Skin Friction Measurement Techniques

Skin friction measurement techniques that were in use at the time of the original wind tunnel test program are shown in Figure 9.

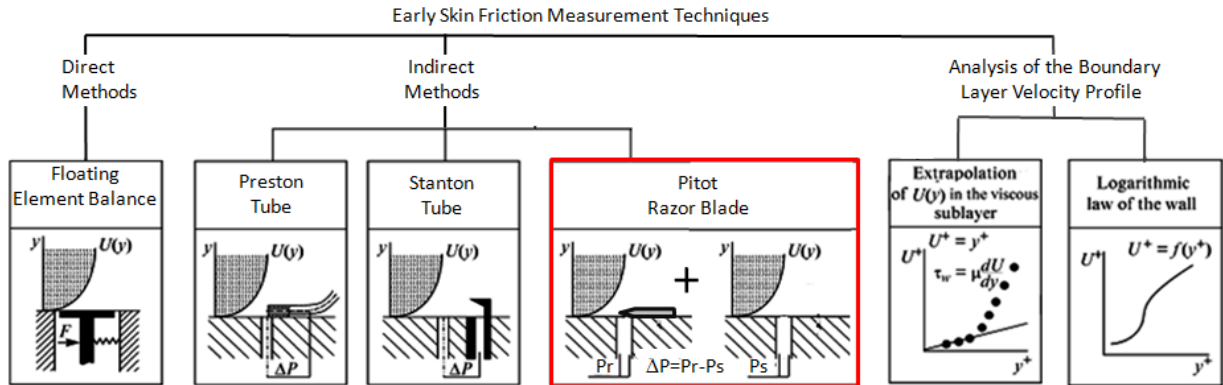


Figure 9: Early Skin Friction Measurement Techniques

These included direct force methods using floating element balances, various indirect methods that relate the local skin friction force to pressure differential measurements very close to the surface in the “law of the wall” region, and methods that attempted to deduce the skin friction from analyses of measured boundary layer velocity profiles.

Floating element measurements are generally considered to be the most accurate and make no assumptions about the nature of the boundary layer. However, the tiny force measurements, flushness requirements, tare corrections make the process of obtaining reliable accurate results extremely difficult. In addition, this technique is generally restricted to a few measurement stations and therefore would not be an appropriate or viable selection for determining the variation of skin friction at a large number of stations along a body. Floating element skin friction measurements have proven to be very useful in establishing the calibration curves used in the indirect methods of determining skin friction.

Skin friction determined from analysis of velocity profile data are generally neither considered to be accurate nor reliable. Indirect methods of determining skin friction consequently were the most commonly used methods and still are often used today. The skin friction on the WSR body was measured by the razor blade technique described in Ref. 6. The razor blade technique shown in figure 10 is an indirect method of determining the local skin friction similar to a Stanton tube or a Preston tube. The technique consists of forming a surface pitot-tube by placing a small segment of razor blade on the surface with its tapered cutting edge above a static-pressure hole.

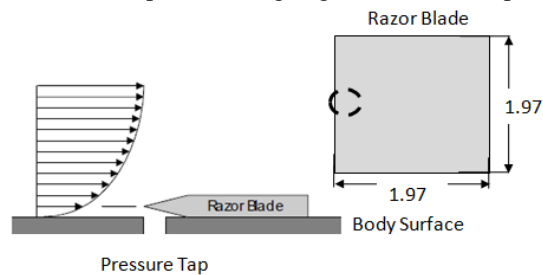


Figure 10: Razor Blade Indirect Skin Friction Measurement

In 1956 Hool⁷ proposed the razor blade technique as a form of a Stanton surface tube in which the 'tube' was formed on the one side by the surface of the model and on the other by the lower side of the tapered cutting edge of a segment of razor blade. The static pressure developed in this small enclosure was measured by a normal static hole in the surface of the model. With the razor blade removed, this same static-pressure hole can be used to measure the undisturbed static pressure and the difference between these two pressure measurements is directly related to the local skin friction.

Hool's calibration methodology was obtained semi-empirically by placing the blade in a laminar flow and can at best only be expected to apply to a turbulent boundary layer if the blade lies wholly within the laminar sub-layer. This restriction is not acceptable for model use where thin turbulent boundary layers can occur. This restriction was

negated and the full potential of this method was established by Smith, Gaudet and Winter⁶ who obtained a calibration in a turbulent supersonic boundary layer.

The indirect skin friction measurement technique is essentially based on the “Law of the Wall” in which the local shear stress is related to local flow properties. The difference in the surface pitot pressure measured with razor blade present and the static pressure without the razor blade, Δp , is related to the local shearing stress, τ .

Assuming a universal inner law (or law of the wall), Δp can be expressed as:

$$\Delta p = \Delta p(\tau, \rho, \mu, \eta) \quad (8)$$

where ρ and μ are the density and viscosity of the fluid and h is the razor-blade height (Figure 8).

Since the universal inner law is assumed to hold, the boundary layer thickness (δ) is not expected to be a relevant independent variable provided that $\delta/h \gg 1$, (reference 5).

The fundamental relationship can be obtained using dimensional analysis as:

$$\frac{\tau h^2 \rho}{\mu^2} = Fn \left(\frac{\Delta p \cdot h^2 \cdot \rho}{\mu^2} \right) \quad (9)$$

The calibration function “Fn” was determined by Smith, Gaudet and Winter⁷ based on direct skin friction measurements. References 8 and 9 contain other detailed information about the razor blade measurement technique.

The specific geometry used for the skin friction measurements as shown in figure 9 included portions of razor blades (about 0.2 inch square) which were mounted over the row of static pressure holes located at $\theta = 30$ degrees. The razor blades were mounted 0.005 inches above the surface of the model. Results obtained by repeating measurements with alternate blades removed established that the presence of the razor blades did not influence the surface pressure measurements at other stations.

For a Reynolds number of 10^7 the pressure coefficients were estimated to have an accuracy of about 0.005. About half of the estimated error was due to possible systematic error and about half due to random error.

The skin-friction coefficients were estimated to be accurate to within ± 0.0002 . Part of the error was due to inaccuracies in measurement and part due to incorrect fore and aft positioning of the blades with respect to the static holes. The errors were estimated to be smaller at the higher Reynolds numbers and larger at the lower Reynolds numbers.

The conventions used in the wind tunnel test program and subsequently also for the computational results presented in this report include:

- C_p , pressure coefficients referenced to free stream static pressure, p_∞ , and free stream dynamic pressure, q_∞

$$C_p = \frac{p - p_\infty}{q_\infty} \quad (10)$$

- C_f^* , local skin-friction coefficient referenced to the local dynamic pressure, q_l
- C_f , local skin friction coefficients referenced to free stream dynamic pressure. The variation of C_f over the length of the body is a direct correlation of the variation of the shear stress over the body.

The conversion of the skin friction data to reference free stream dynamic pressure was obtained by the transformation shown in equation 11.

$$C_f = C_f^* \frac{q_l}{q_\infty} = \frac{p_l}{p_\infty} \left(\frac{M_l}{M_\infty} \right)^2 = C_f^* \cdot (0.7 \cdot C_p \cdot M_\infty^2 + 1) \cdot \left(\frac{M_l}{M_\infty} \right)^2 \quad (11)$$

The free stream skin friction coefficient, C_f , was integrated over the length of the body between the first pressure port station, ψ_{LOW} , to the last pressure port station, ψ_{HI} to obtain an average skin friction coefficient CF , as defined in equation 12.

$$CF(\psi) = \frac{\int_{\psi_{LOW}}^{\psi} Cf(\psi) d\psi}{\psi - \psi_{LOW}} \quad \text{for } \psi \leq \psi_{HI} \quad (12)$$

The product of the free stream local skin friction coefficient times the local body circumference was integrated to obtain a distribution of viscous drag, CDV, between ψ_{LOW} and ψ_{HI} using equation 13.

$$CDV(\psi) = \frac{2\pi L_B^2}{A_{BASE}} \int_{\psi_{LOW}}^{\psi} Cf(\psi) \cdot R_B(\psi) d\psi \quad \text{for } \psi \leq \psi_{HI} \quad (13)$$

L_B = Body Length

A_{BASE} = Body base area.

R_B = Local body radius

ψ = non dimensional body station, x/L_B

V. TRANAIR CFD Program

The TRANAIR computer program^{10, 11} calculates transonic flow about arbitrary configurations at subsonic, transonic and supersonic free stream Mach numbers. TRANAIR solves the nonlinear full potential equation subject to a variety of boundary conditions, modeling wakes, inlets, exhausts, porous walls, and impermeable surfaces. The calculation method employs a unique Cartesian adaptive gridding technique. Viscous effects are modeled using an integral boundary layer code^{12, 13} which was developed by Remark Drela. Because of its user friendliness, robustness and reliability, the TRANAIR program is widely used within Boeing for a wide variety of design optimization, analysis and predictive type studies covering a wide range of flow conditions for airplane design, development and assessments. The TRANAIR program is commercially available as TRANAIR ++ from the Calmar Research Corp.

Figure 11 shows typical WSR body TRANAIR adapted computational grids for a subsonic analysis condition and for a supersonic analysis condition.

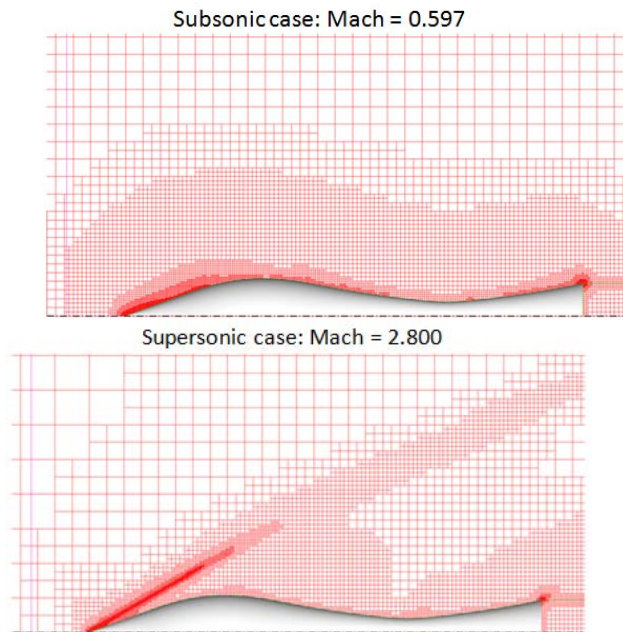


Figure 11: TRANAIR Typical Analysis Grids

TRANAIR analyses were made for all of the reported test conditions. Predicted local Mach number distributions, pressure distributions and local skin friction distributions are compared with the corresponding test data along the

length of the body. Theoretical predictions of boundary layer growth parameters including the displacement thickness, δ^* , momentum thickness, θ , and shape factor, H , are also compared with the test data. Calculated boundary layer thickness distributions, δ , are added to outlines of the test geometry and are compared with the indicated boundary layer in the experimental schlieren pictures. The TRANAIR calculations, unless otherwise noted, were all made with transition specified to occur at 2.5% of the body length. This corresponds to the boundary layer trip location on the wind tunnel model.

The test data includes numerous measured velocity profiles for each of the test conditions. The use of these data in this study was indirectly in the form of the integrated boundary layer parameters, δ^* , θ and H .

VI. Subsonic Analyses Results

Results of the subsonic analyses and comparisons with the corresponding test data are shown in Figures 12 through 20. The theoretical local Mach number distribution around the WSR body is shown in figure 12.

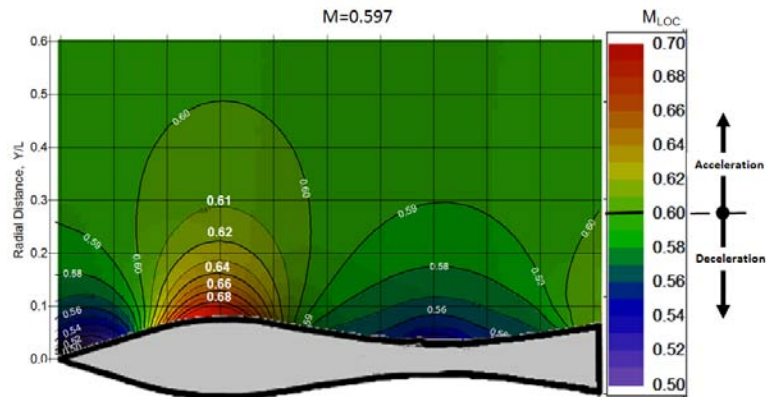


Figure 12: Predicted local Mach number distribution for Mach = 0.597

The divergent streamlines from the nose to the maximum area station together with a favorable pressure gradient results in acceleration of the flow. From the maximum area station to the minimum area station the streamlines are convergent and the pressure gradient is unfavorable and hence the flow is decelerated. From the minimum area station until the end of the body the flow is divergent with a slightly favorable pressure gradient resulting in a slightly accelerated flow. Comparisons of surface local Mach number, M_{Loc} , pressure coefficient, C_p , distributions are shown in figure 13. The theoretical CFD predictions were made with a boundary layer transition body station, x_t/L , at 2.5% of the body length corresponding to the experimental trip location.

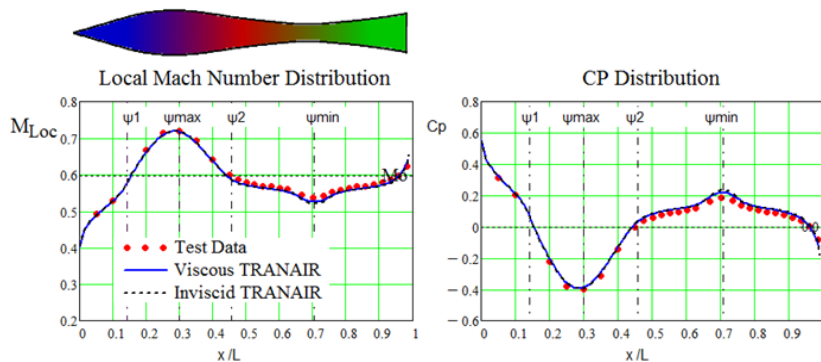


Figure 13: Mach Number and C_p Distributions for Mach 0.597, $Re_l = 9.85 \times 10^6$ and $x_t/L = 0.025$

The predicted M_{Loc} and C_p distributions agree quite closely with the test. However the theoretical pressure coefficient predictions appear to be slightly higher than the test data. The inviscid and viscous C_p and M_{Loc} distributions are essentially identical which indicates that the predicted boundary layer had no discernible effect on the pressure distribution.

The experimental and theoretical pressure coefficient distributions were used to obtain the local pressure drag distribution as given by equation 14 and the integrated pressure drag distribution as given by equation 15.

$$\frac{dCDP(\psi)}{d\psi} = \frac{2 \cdot \pi \cdot L^2}{A} C_p(\psi) \rho(\psi) \frac{d\rho(\psi)}{d\psi} \quad (14)$$

$$CDP(\psi) = \int_{\psi_{LOW}}^{\psi_{HI}} \frac{dCDP(\psi)}{d\psi} d\psi \quad (15)$$

The experimental and theoretical pressure drag distributions and the integrated pressure drag distributions are shown in figure 14. As is typical for flow at subsonic Mach numbers^{1,2}, there are regions of rather large positive and negative local pressure drag distributions. Consequently, the total pressure drag is seen to be the small difference between these large positive and negative drag regions.

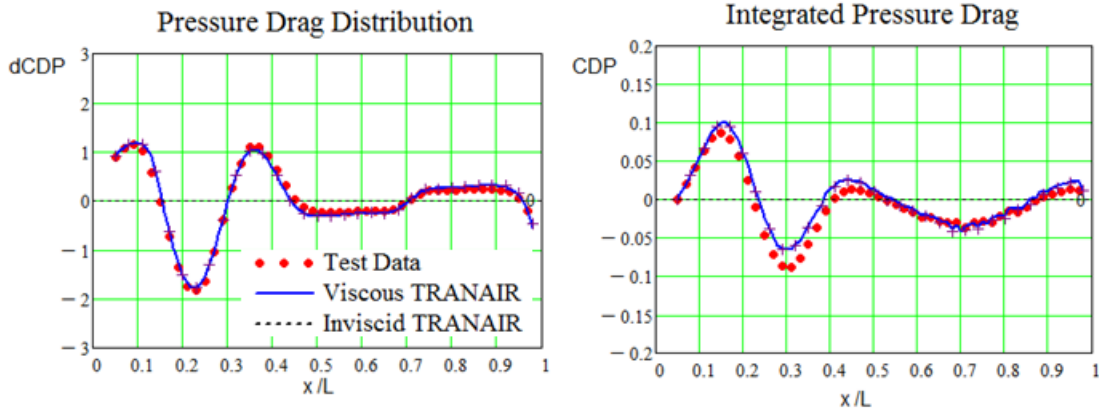


Figure 14: Pressure Drag for Mach 0.597, Rel = 9.85×10^6 and $xt/L = 0.025$

The local skin friction, average skin friction and integrated viscous drag distributions are shown in figure 15. The local skin friction is seen to increase in the divergence region from the nose to slightly before the maximum area station. The skin local skin friction then rapidly decreases in the convergence region down to the minimum body area station as the local Mach number is reduced.

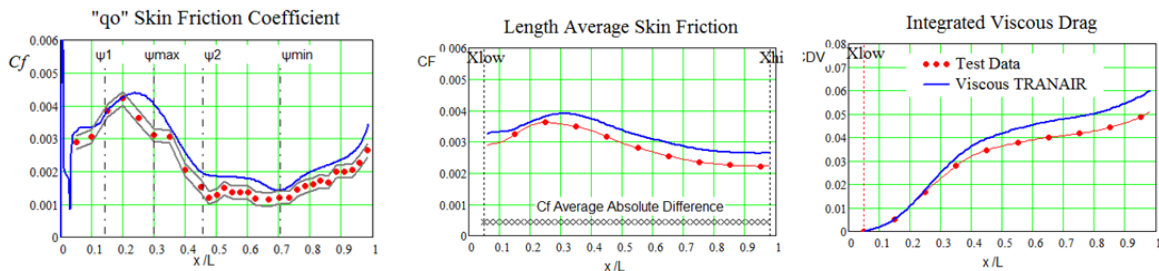


Figure 15: Viscous drag for Mach 0.597, Rel = 9.85×10^6 and $xt/L = 0.025$

The experimental skin friction data includes the estimated error band of ± 0.0002 . The predicted C_f distributions are quite similar to the test data. Integrated average skin friction and viscous drag distributions over the length of the experimental data, are also shown in the figure. The integrated skin friction distributions were computed as a means to qualitatively assess the impact of the differences between the experimental and measured skin friction.

Comparisons of experimental and theoretical integrated boundary layer growth parameters are shown in figure 16. These data include displacement thickness, δ^* , momentum thickness, θ , and shape factor, H. The experimental boundary layer growth parameters were obtained by integrations of the velocity profiles at the measurement body stations.

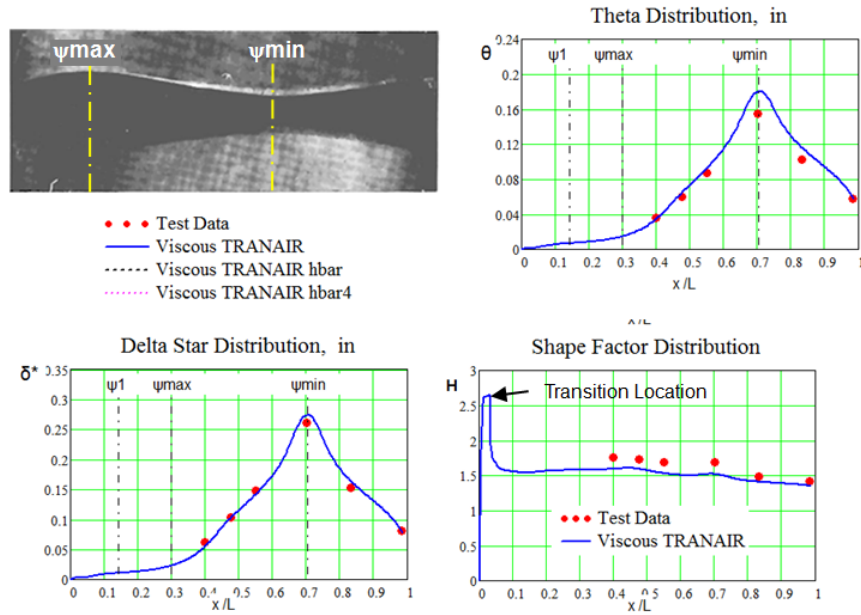


Figure 16: Boundary Layer Analyses for Mach 0.597, $Re_l = 9.85 \times 10^6$ and $xt/L = 0.025$

The theoretical predictions are remarkably close to the experimental data, especially when considering the rather complicated flow field consisting of regions of streamline convergence and divergence plus regions of favorable and unfavorable pressure gradients. It is seen that there is a rapid growth in the boundary layer thickness parameters, δ^* and θ from the maximum area station to the minimum area station followed by an equally rapid decrease in boundary layer thickness from the minimum area station to the end of the body

The predicted local Mach number distribution around the WSR body at an increased Mach number of 0.801 is shown in figure 17.

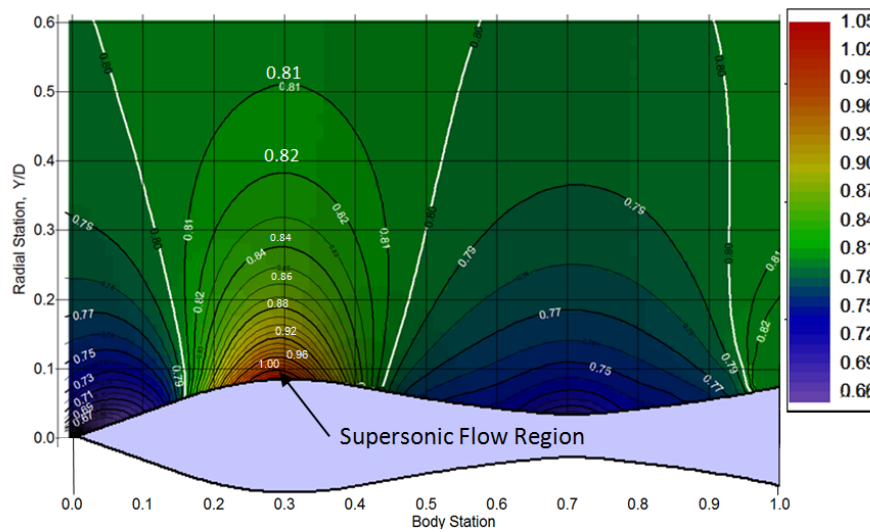


Figure 17: Mach = 0.801 Flow Field Mach Number Distribution

The acceleration of the flow up to the maximum area station results in a small region of embedded supersonic flow centered about the maximum area station.

Figure 18 contains comparisons of the theoretical and experimental local Mach number and pressure coefficient distributions for this test condition.

The theoretical Mach number and Cp distributions agree closely with the test data.

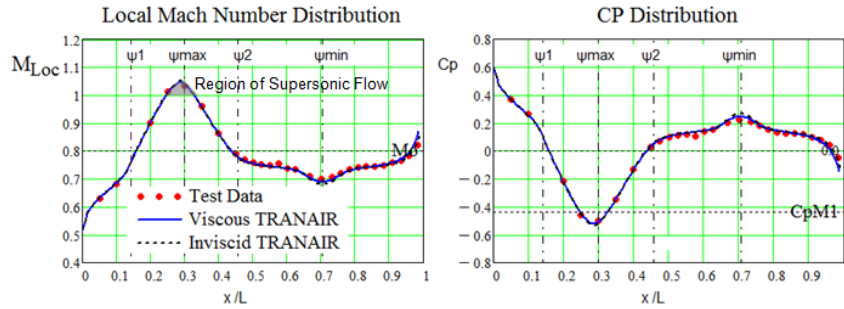


Figure 18: Mach Number and Cp Distributions for Mach 0.801, $Re_l = 9.88 \times 10^6$ and $x_t/L = 0.025$

The local pressure drag and integrated drag distributions are shown in figure 19. The theoretical predictions closely match the test data. Once again, the net pressure drag is the rather small difference between large positive and negative drag regions.

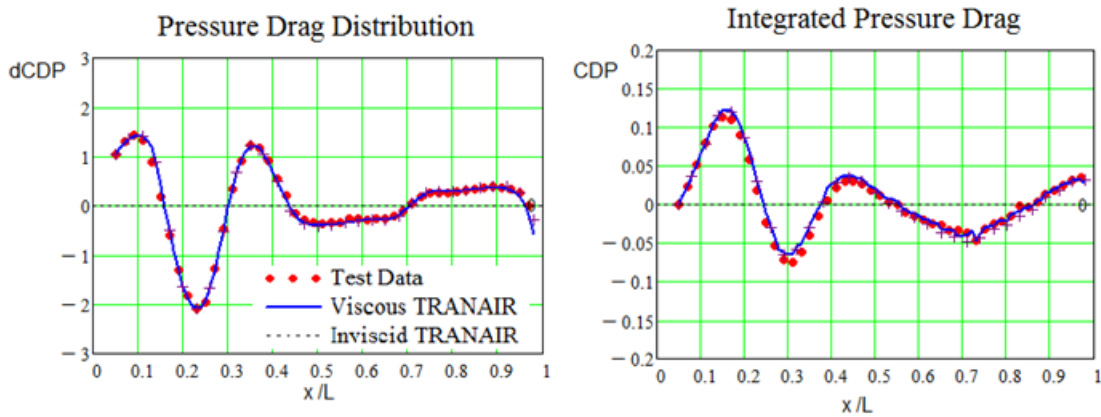


Figure 19: Pressure drag for Mach 0.801, $Re_l = 9.88 \times 10^6$ and $x_t/L = 0.025$

The local skin friction distributions as shown in figure 20 are quite similar to the test measurements with theory slightly over predicting the integrated skin friction data.

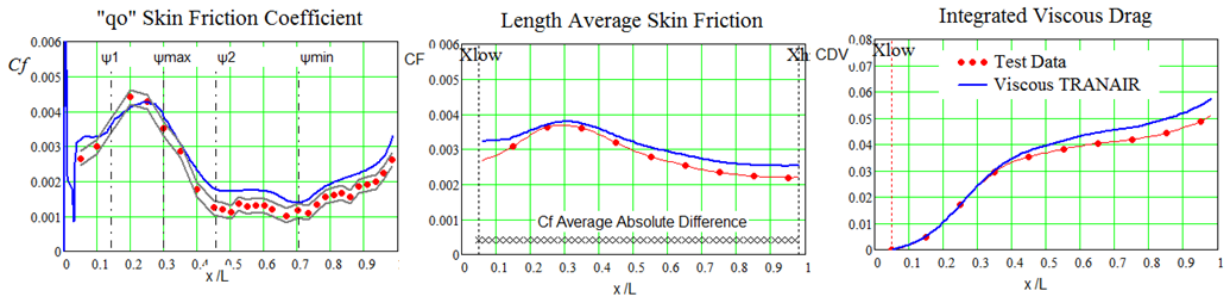


Figure 20: Skin Friction and Viscous Drag Analyses for Mach 0.801, $Re_l = 9.98 \times 10^6$ and $x_t/L = 0.025$

There were no measured velocity profiles and hence no experimental boundary layer growth parameters for this test condition. Predicted boundary layer growth parameters are shown in figure 21. This figure also contains a comparison of the experimental boundary layer thickness as evident in the schlieren picture, with the predicted boundary layer thickness. The overlaid theoretical boundary layer appears to match the experimental boundary layer thickness quite well.

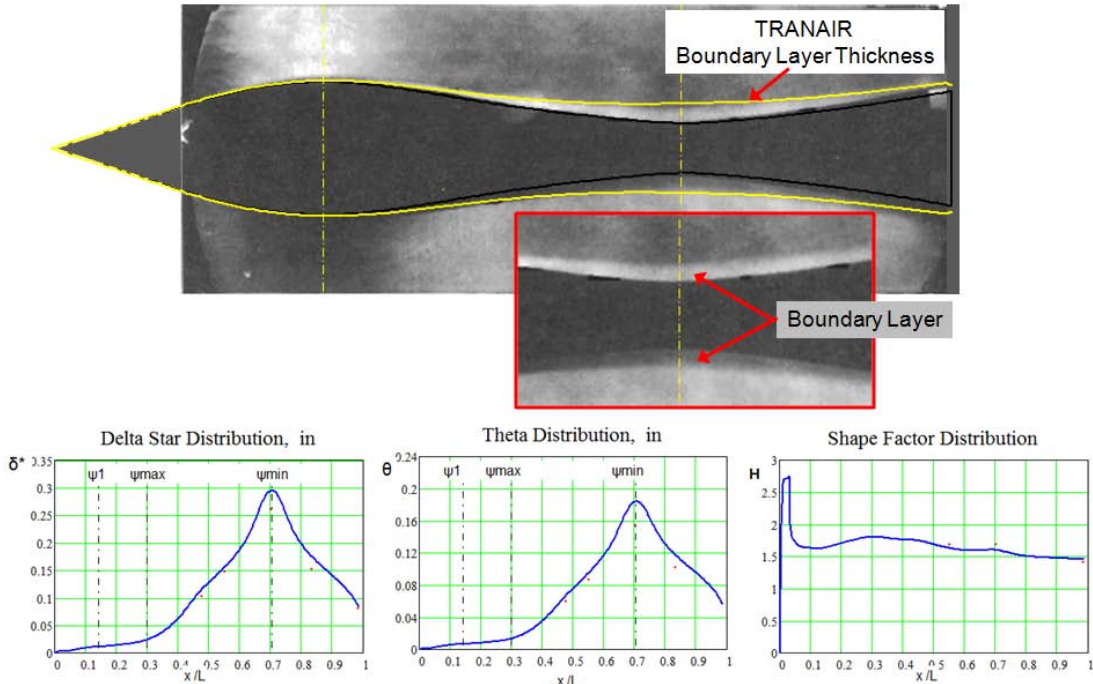


Figure 21: TRANAIR Boundary Layer Predictions for Mach 0.801, $Rel = 9.98 \times 10^6$ and $xt/L = 0.025$

VII. Supersonic Analyses Results for Mach ≈ 1.4

Experimental data were obtained at Mach = 1.4 for three different Reynolds numbers of approximately 5×10^6 , 10^7 and 2×10^7 . The experimental local Mach number, pressure coefficient and local skin friction distributions are compared with the corresponding TRANAIR predictions in figure 22. The theoretical predictions were obtained with a specified transition location at 2.5% of the body length

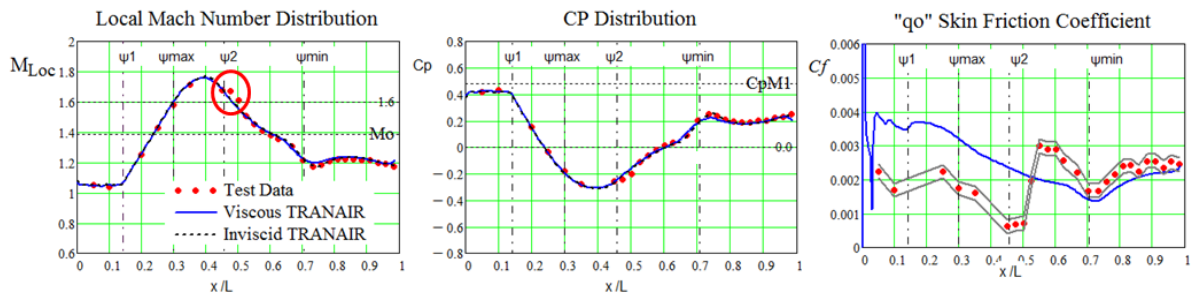


Figure 22: Skin Friction and Cp Analyses for Mach 1.390, $Rel = 5.04 \times 10^6$ and $xt/L = 0.025$

The experimental skin friction distribution implies that the body boundary layer trip at $xt/L = 0.025$ was totally ineffective. It would appear that transition occurred on the model somewhere between 44% to 50% of the body length. The very low values of C_f indicate that in this region the flow was close to separation.

TRANAIR analyses were then made with a specified aft transition location of $xt/L = 0.50$. The inherent transition methodology within TRANAIR however determined that transition would occur at $xt/L = 0.44$. Consequently the theoretical analysis corresponded to a trips free analysis. The comparative results of the trips free analyses are shown in figures 23, 24 and 25. The predicted local Mach number and pressure coefficient distributions agree quite well with the test data as shown in figure 23.

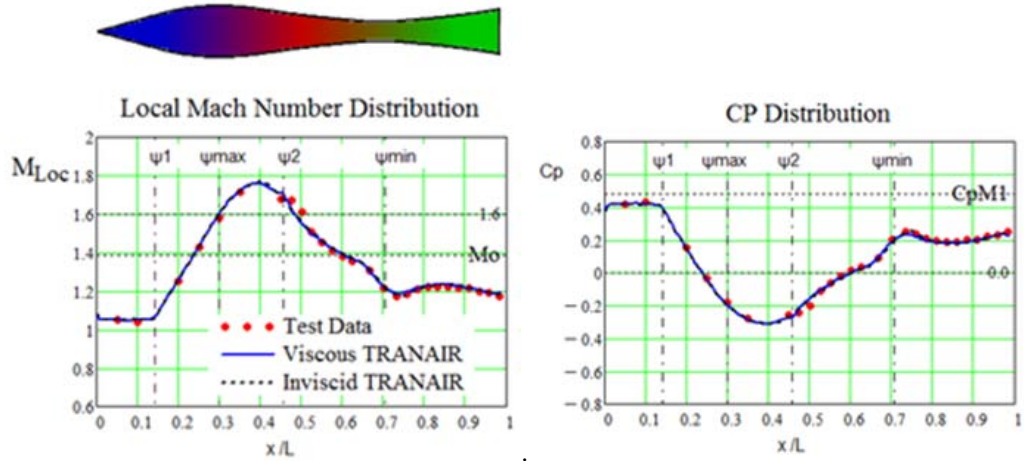


Figure 23: Mach Number and C_f Trip Free Analyses for Mach 1.390, $Rel = 5.04 \times 10^6$

Contrary to the previously shown subsonic comparisons, the flow continues to accelerate beyond the maximum area location, which occurs at the 30% body station, well into the convergence region until the pressure gradient changes from favorable to unfavorable which occurs at approximately the 40% body station.

The pressure drag and integrated pressure drag distribution comparisons as shown in figure 24 are in very good agreement with the test data.

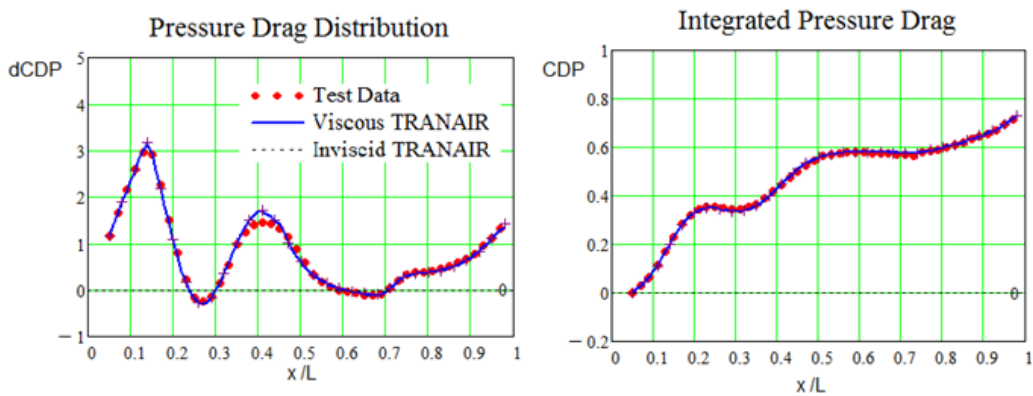


Figure 24: Pressure Drag Trip Free Analyses for Mach 1.390, $Rel = 5.04 \times 10^6$

The theoretical C_f results obtained with the aft trip locations as shown in figure 25, appear to be quite similar to the test data.

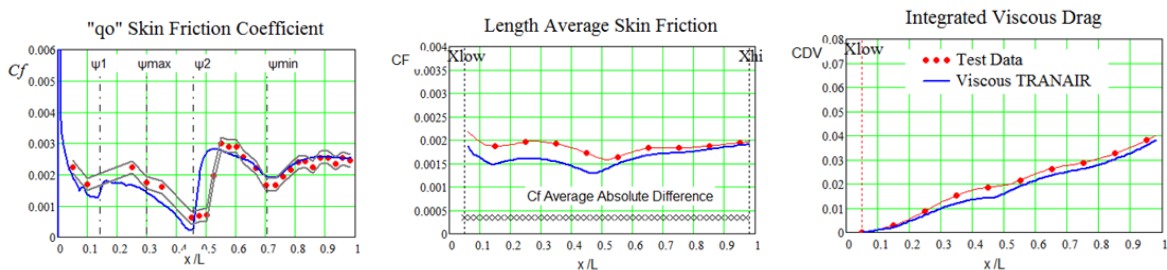


Figure 25: Trip Free Pressure Drag and Viscous Drag Analyses for Mach 1.390, $Rel = 5.04 \times 10^6$

The laminar flow predictions from the nose up to the boundary layer transition region are slightly less than the test data. The experimental transition region appears to be a bit wider than that predicted by the theoretical model. The local skin friction near the minimum area station and on the aft flared body is accurately predicted.

For most of the body, the predicted average skin friction coefficient is less than the test data. The overall average skin friction, however, at the end of the body is in excellent agreement with the test data. The average skin friction distribution figure also shows the magnitude of the average absolute Cf difference between the predicted and theoretical local skin friction values, $|\Delta Cf|_{Ave}$ which is defined by equation 16.

$$|\Delta Cf|_{Ave} = \frac{1}{N} \sum_{i=1}^N |Cf_{Exp} - Cf_{Theory}| \quad (16)$$

N = total number of experimental data points

Cf_{Exp} = Experimental local skin friction measurements

Cf_{Theory} = Corresponding theoretical local skin friction predictions

For this case, the average absolute Cf difference is equal in magnitude to 17.2% of the overall average skin friction coefficient at the end of the body even though the difference between the total experiment viscous drag and the theoretical viscous drag prediction is less than 5 %.

Velocity profile measurements were not obtained at this Reynolds number, however, the theoretical predictions of the boundary layer growth parameters for the forward and aft trip locations are shown in figure 26. The boundary layer growth parameters are seen to be quite sensitive to transition location. The long run of laminar flow for the trip free location resulted in a significant reduction in both that displacement thickness, δ^* , and the momentum thickness, θ . The location of transition is clearly evident by the sudden break in the shape factor, H.

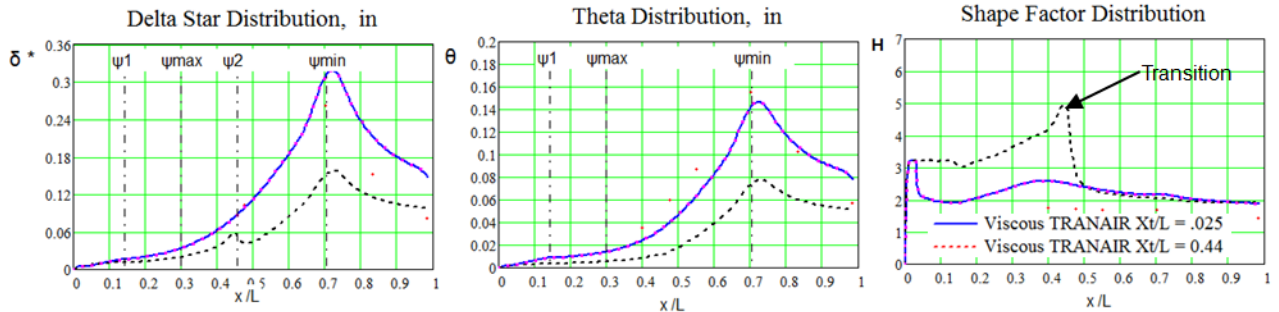


Figure 26: Predicted Effects of Transition Location for Mach 1.390, Rel = 5.04×10⁶

The results of the TRANAIR analyses of the WSR body at a Reynolds number of approximately 10 million are shown in figures 27, 28, 29 and 30. The predicted pressure distribution shown in figure 27 agrees closely with the test data. Consequently the predicted pressure drag distribution and the pressure drag shown in figure 28, closely match the test data

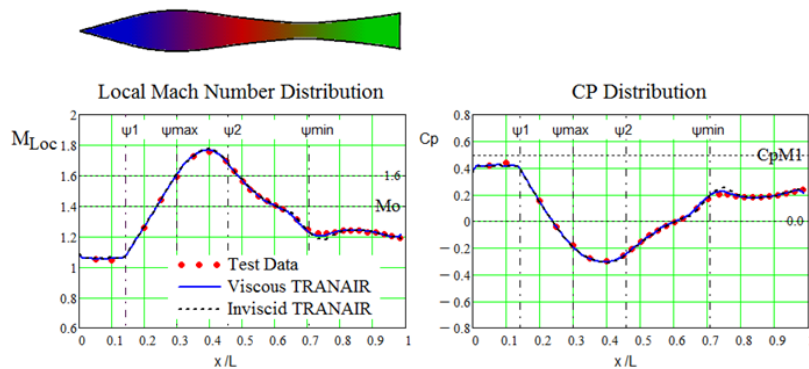


Figure 27: CP and Mach Number Distributions for Mach 1.398, Rel = 10.02×10⁶ and xt/L = 0.025

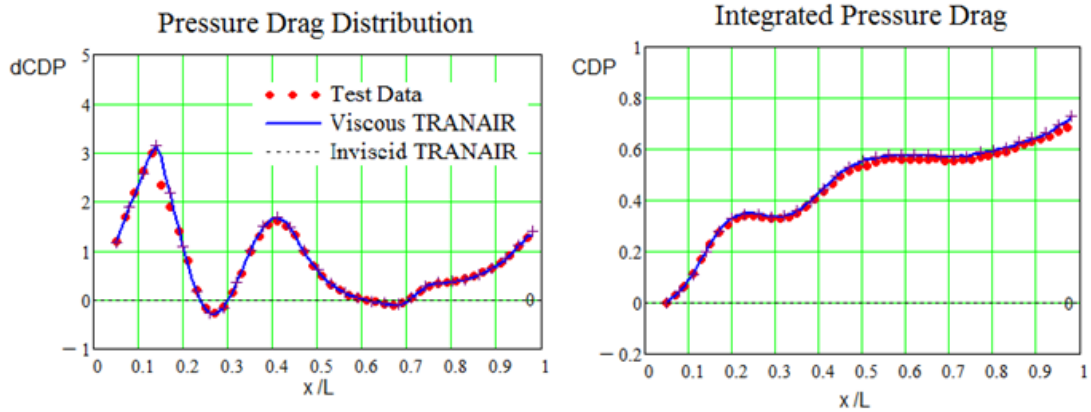


Figure 28: Pressure Drag Analyses for Mach 1.398, $Re = 10.02 \times 10^6$ and $x_t/L = 0.025$

The shapes of the theoretical and experimental skin friction distributions in figure 29 are quite similar. The theoretical local skin friction predictions however are less than experiment over the front half of the body and somewhat greater than experiment over the last half of the body. The predicted and experimental distributions of the average skin friction reflect these differences. The predicted average skin friction and viscous drag values at the end of the body, however, are equal to the experimental values even though average absolute local skin friction difference is equal to approximately 13 % of the total average skin friction.

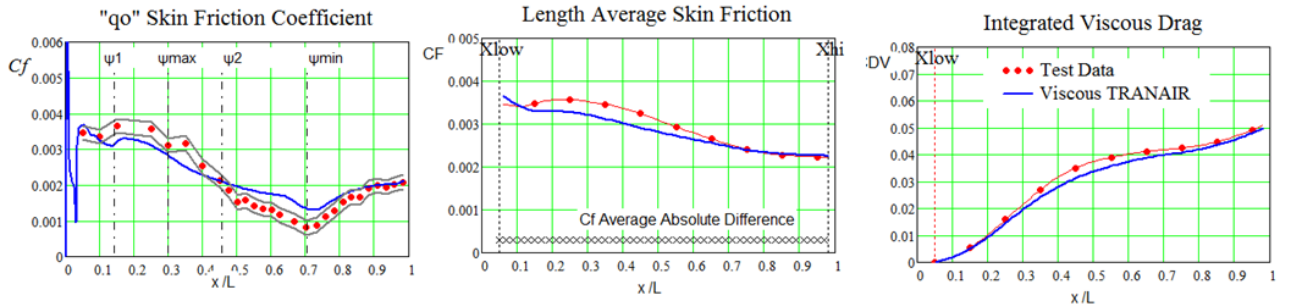


Figure 29: Skin Friction and Viscous Drag Analyses for Mach 1.398, $Re = 10.02 \times 10^6$ and $x_t/L = 0.025$

Predictions of the boundary layer growth parameters are compared with the test data in figure 30. The predicted edge of the boundary layer matched the indicated boundary layer thickness in the schlieren picture.

The predicted displacement thickness, momentum thickness and shape factor closely matches the test data.

The boundary layer is seen to grow very rapidly starting at the maximum radius station due to the flow convergence and adverse pressure gradient and reaches a peak thickness at the minimum area station. The boundary thickness then reduces rather rapidly to the end of the body because of the combined effect of flow divergence and a slightly adverse pressure gradient.

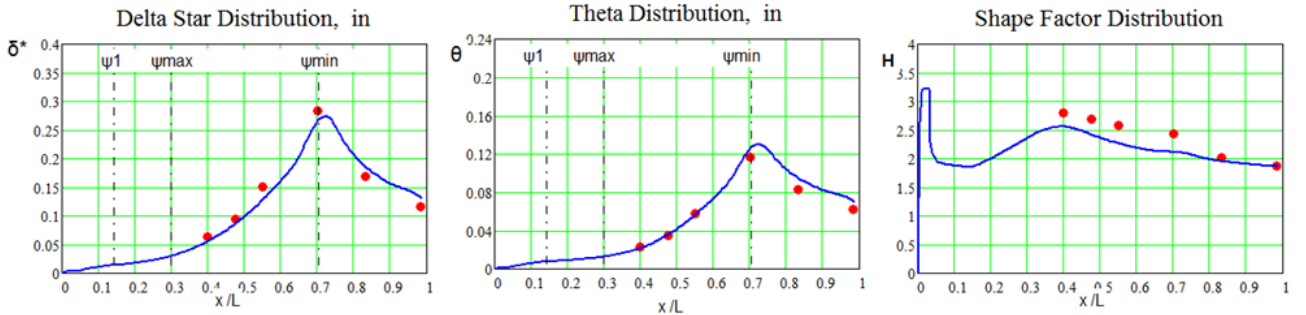
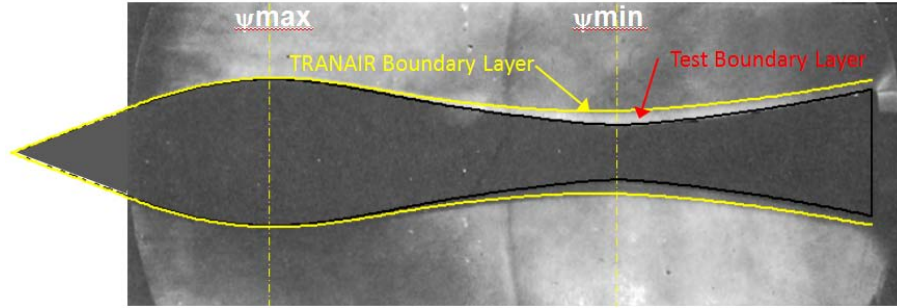


Figure 30: Boundary Layer Analyses for Mach 1.398, $Re_l = 10.02 \times 10^6$ and $xt/L = 0.025$

Results obtained at a Reynolds number of approximately 2×10^7 are shown in figure 31, 32 and 33.

The computed and experimental pressure distributions are essentially the same, consequently the predicted pressure drag also matches the test data.

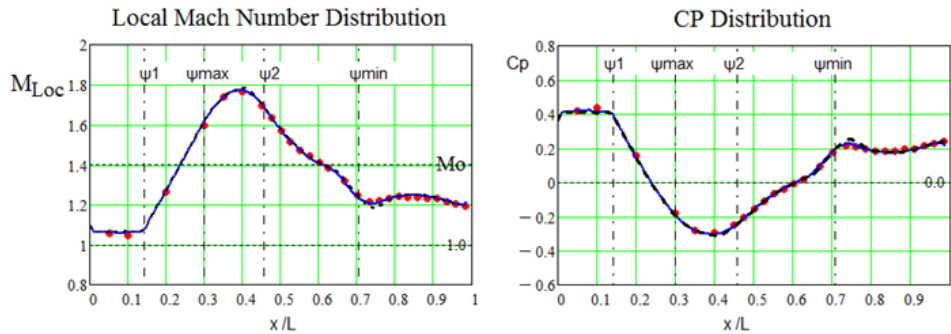


Figure 31: Mach Number and C_p Analyses for Mach 1.404, $Re_l = 19.97 \times 10^6$ and $xt/L = 0.025$

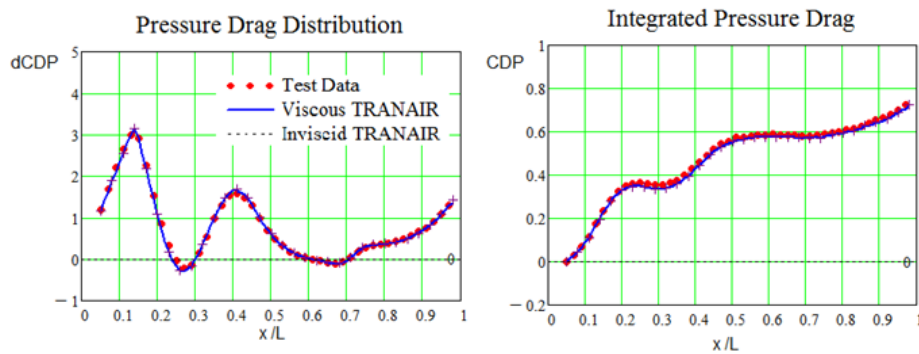


Figure 32: Pressure Drag Analyses for Mach 1.404, $Re_l = 19.97 \times 10^6$ and $xt/L = 0.025$

The predicted skin friction distribution is less than the test data in the divergent flow region and then becomes larger than experiment aft of station ψ_2 in the convergent flow region up the aft body flare area.

The predicted average skin friction and the viscous drag matched experiment as a result of the compensating positive and negative local skin friction differences over the body length.

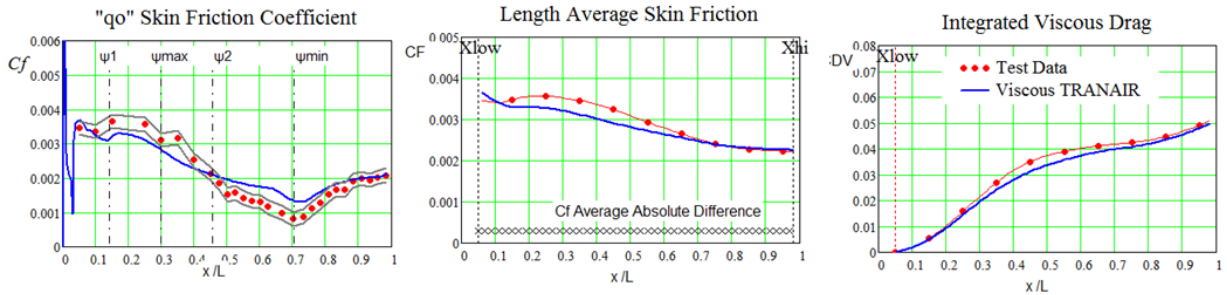


Figure 33: Skin Friction and Cp Analyses for Mach 1.404, Rel = 19.97×10^6 and $x_t/L = 0.025$

The predicted boundary layer growth values of δ^* , θ and H closely match the test data as shown in figure 34.

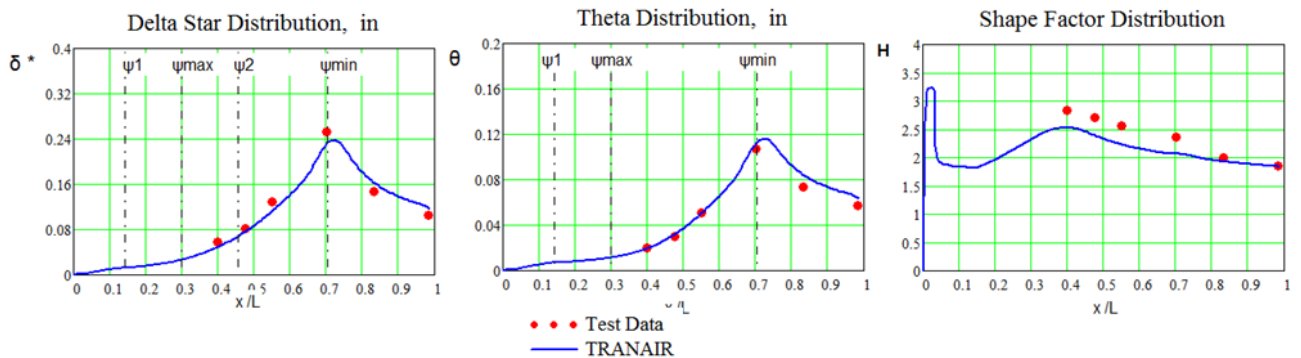


Figure 34: Boundary Layer Analyses for Mach 1.404, Rel = 19.97×10^6 and $x_t/L = 0.025$

VIII. Boundary Layer Transition Study

A theoretical boundary layer transition study was made in order to gain a better understanding between the relation between boundary layer transition location and laminar separation on the WSR body. The analyses were made for a Reynolds number of 5×10^6 and a Mach number of 1.4. Three additional transition stations were evaluated between the forward transition location of $x_t/L = 0.025$ and an aft transition location of $x_t/L = 0.44$. This was the maximum transition location for which TRANAIR provided a solution before its prediction methodology resulted in transition. The results are shown in Figure 35.

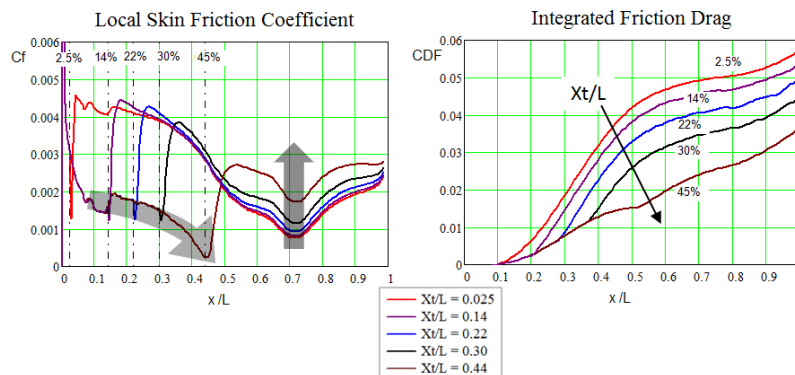


Figure 35: Effect of Transition Location on Skin Friction for Mach = 1.390 and Rel = 5×10^6

The local skin friction reaches minimums in two locations. These include the station for which transition occurs and also at the minimum area station. The local Cf value at the minimum area station increases as the transition

moves aft. The minimum C_f at the transition station however, decreases rather rapidly as the transition station moves aft. The extrapolated results suggest that laminar boundary layer would indeed separate if the transition station moved beyond $x_t/L = 0.44$ to $x_t/L = 0.50$. However as previously discussed, both the experimental flow and the theoretical flow transition slightly before boundary layer separation could occur.

Figure 35 also shows how the integrated skin friction decreased with aft movement of the transition station.

The effect of the boundary layer transition station on the displacement thickness, the momentum thickness and the shape factor distributions are shown in figure 36.

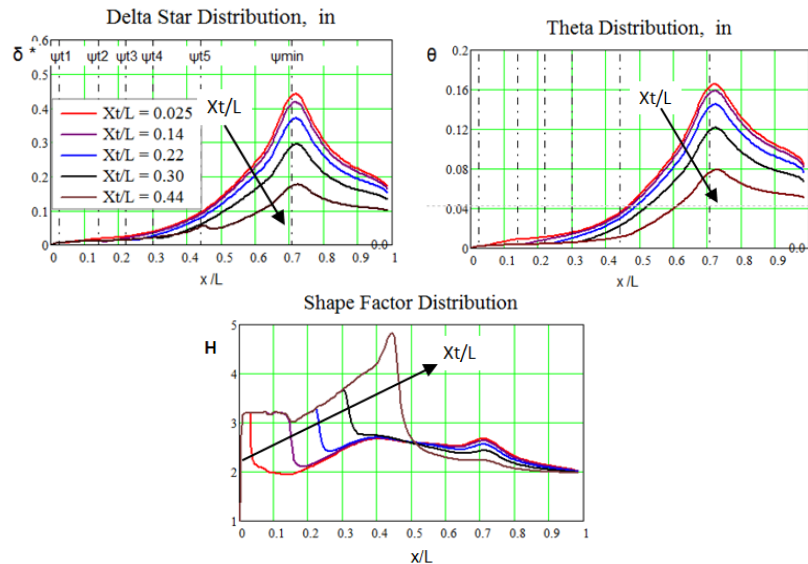


Figure 35: Effect of Transition Location on Boundary Layer Growth Mach = 1.390 and $Re_l = 5 \times 10^6$

The displacement thickness and the momentum thickness decrease rather rapidly with the aft movement of the transition station. The peak value of the shape factor which occurs at the transition station increases with the aft movement of the transition station.

IX. Supersonic Analyses Results for Mach ≈ 1.7

TRANAIR predictions are compared with the test data in figures 34 through 37 for Mach = 1.7 and a Reynolds number of approximately 10^7 .

The pressure distribution and consequently the pressure drag predictions agree very well with the test data.

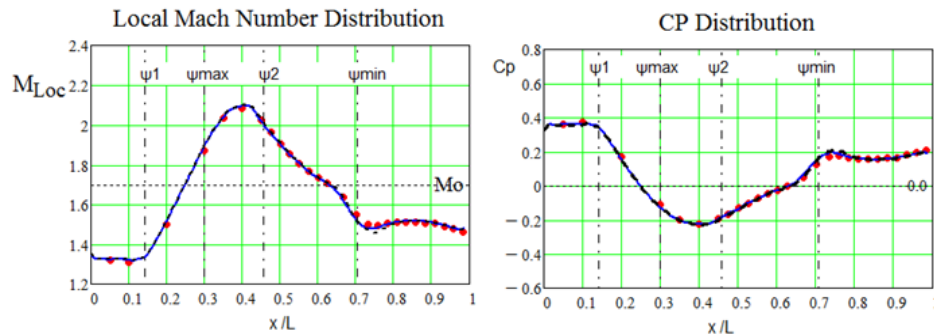


Figure 34: Skin Friction and C_p Analyses for Mach 1.700, $Re_l = 10.03 \times 10^6$ and $x_t/L = 0.025$

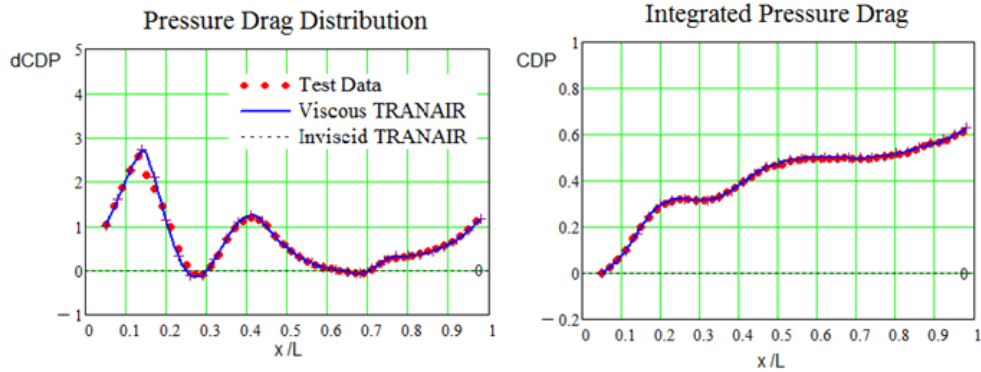


Figure 35: Pressure Drag Analyses for Mach 1.700, $Re_l = 10.03 \times 10^6$ and $x_t/L = 0.025$

The predicted local skin friction is less than the test data in the divergent flow region up to the maximum area station, ψ_{max} and then becomes greater than experiment through much of the convergent flow region down to the minimum area station. The predicted increase in skin friction in the divergent flow region on the aft body flare is less than indicated by experiment. Once again the positive and negative differences between predicted and local skin friction values are self canceling resulting with good agreement between predicted and experimental local skin friction and viscous drag at the end of the body.

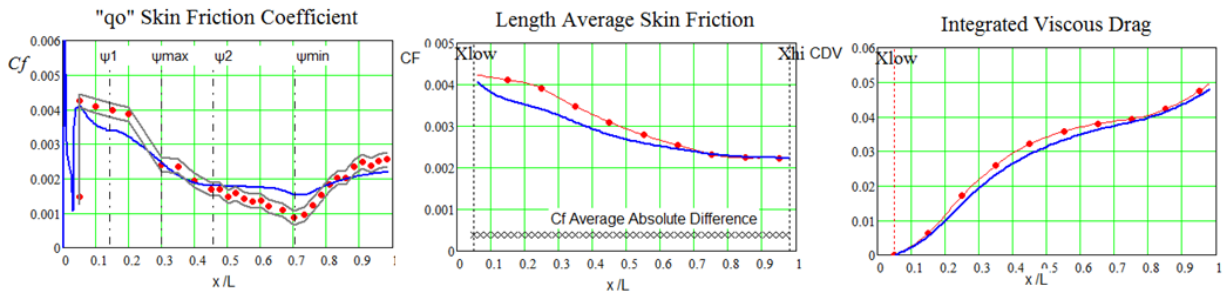


Figure 36: Skin Friction and Viscous Drag Analyses for Mach 1.700, $Re_l = 10.03 \times 10^6$ and $x_t/L = 0.025$

The predicted boundary layer thickness appears to match experiment as shown in figure 37. The predicted displacement thickness, momentum thickness and shape factor distributions are in good agreement with the test data as shown in figure 37.

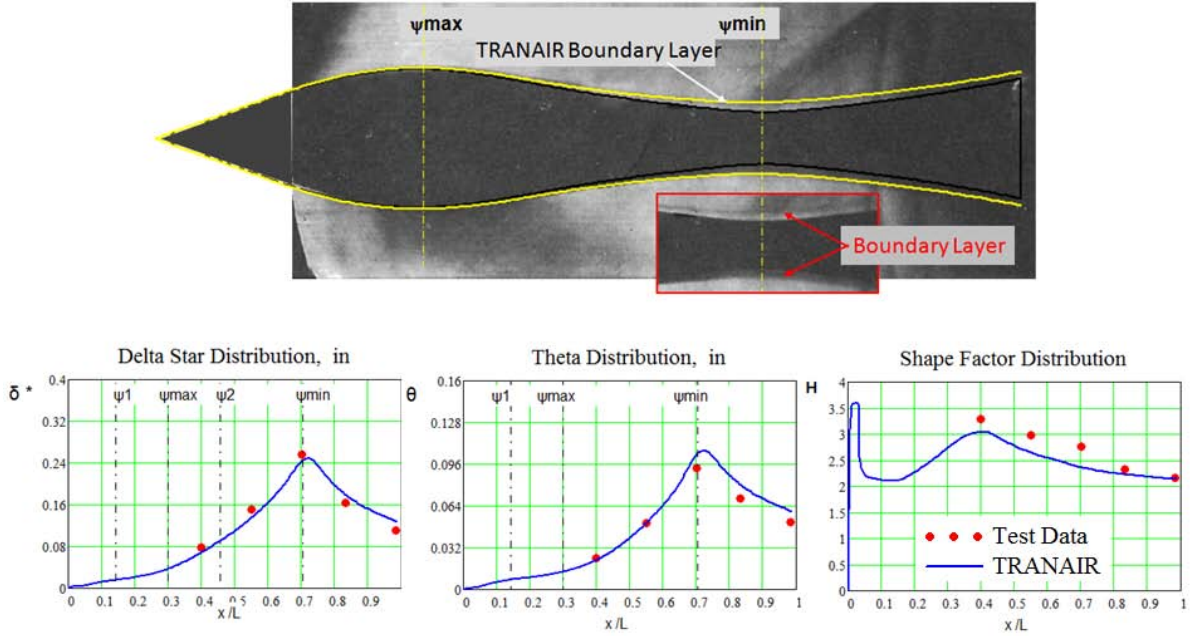


Figure 37: Boundary Layer Analyses for Mach 1.700, $Re_l = 10.03 \times 10^6$ and $x_t/L = 0.025$

X. Supersonic Analyses Results for Mach ≈ 2.0

The flow field pressure distribution around the body for a free stream Mach number of 2.0 is shown in figure 38. Expansion over the maximum area results in a region of high supersonic flow. The flow divergence near the aft end of the body results in local Mach number flow that is less than the free stream number.

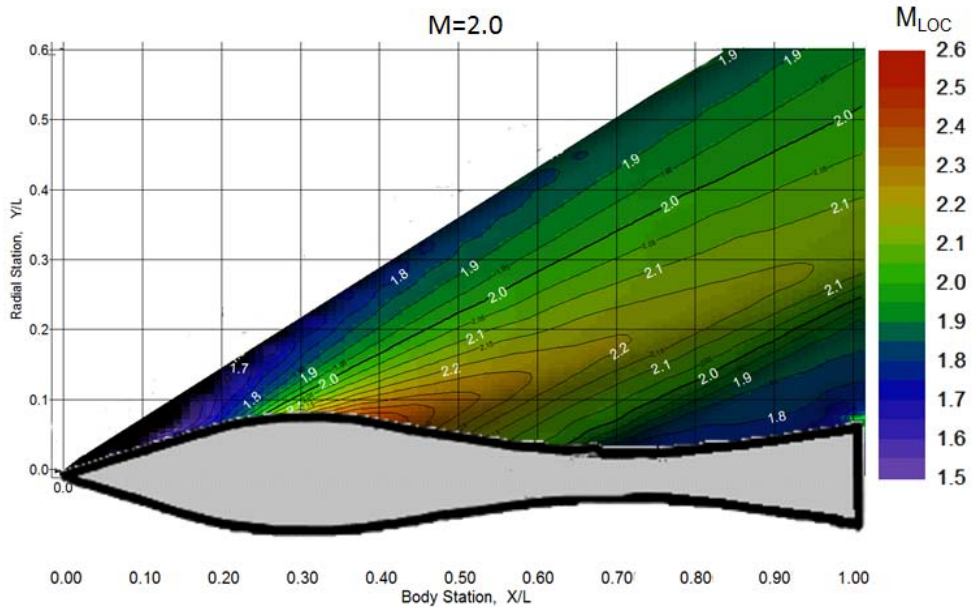


Figure 38: Mach = 2.000 Flow Field Mach Number Distribution

The results show that the experimental test trip strip located at $x_t/L = 0.025$ was not effective at the low test Reynolds number of approximately 5×10^6 . Consequently the theoretical predictions obtained with $x_t/L = 0.025$ are substantially different than the test data as shown in figure 38.

The minimum experimental skin friction levels are close to zero indicating that the flow was close to a condition of laminar flow separation.

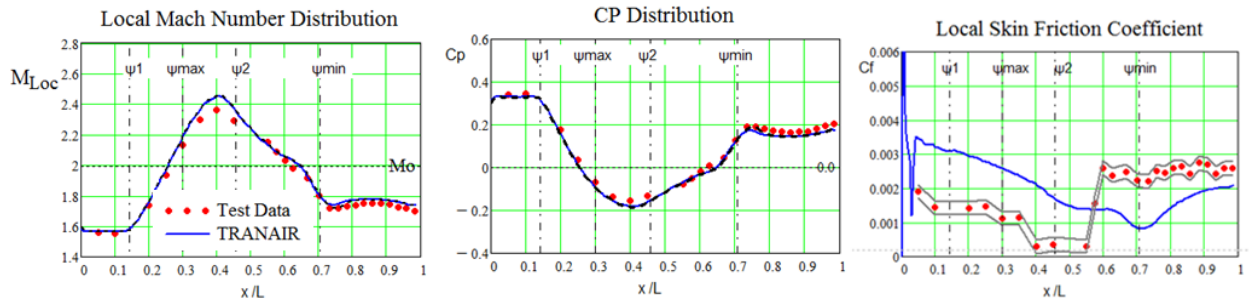


Figure 39: Skin Friction and Cp Analyses for Mach 1.996, Rel = 4.98×10^6 and $x_t/L = 0.025$

A TRANAIR analysis was made with a prescribed boundary layer transition location of $x_t/L = 0.55$. The results are shown in figures 40 and 41. Once again the TRANAIR analysis methodology resulted in a transition location of approximately $x_t/L = 0.44$ which is close to the experimental boundary layer transition location..

The TRANAIR CP predictions match the test data except near the aft end flow divergence region where the theoretical CPs are slightly less than experiment.

The TRANAIR Cf predictions closely match the test data up to the boundary layer TRANSITION region. The theoretical local skin friction values are less than experiment near the aft region of the body. Because of compensating differences, the predicted total viscous drag matches the experimental value.

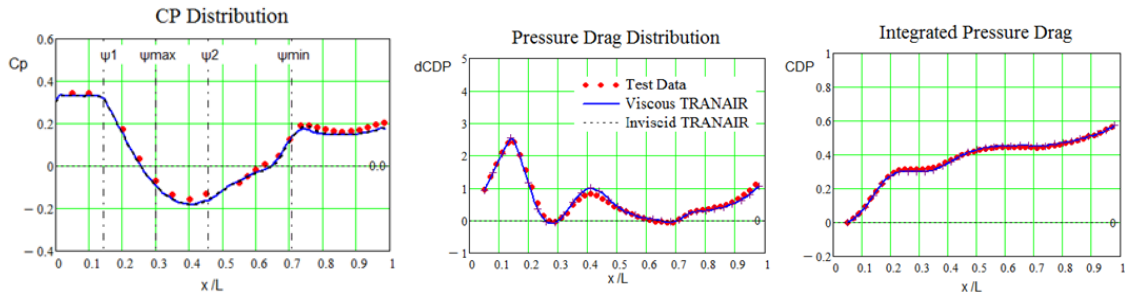


Figure 40: Cp and Pressure Drag Trip Free Analyses for Mach 1.996, Rel = 4.98×10^6

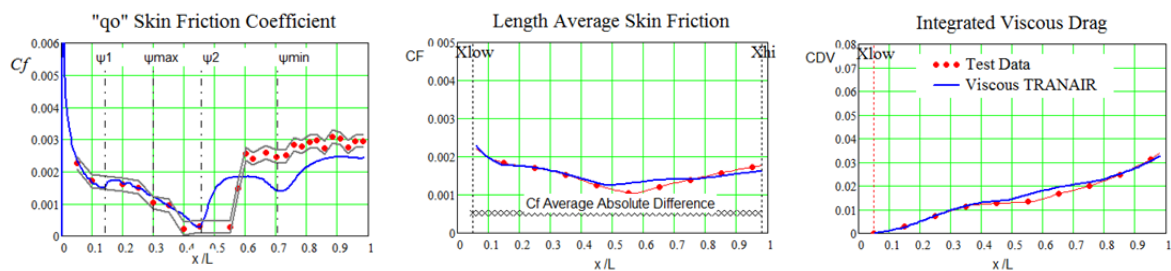


Figure 41: Skin Friction and Viscous Drag Trip Free Analyses for Mach 1.996, Rel = 4.98×10^6

Results from a TRANAIR analysis at a Reynolds number of approximately 10^7 are shown in Figures 42 through 45. The predicted pressure distribution matches experiment along the entire body length. Consequently the pressure drag is accurately predicted by the theory.

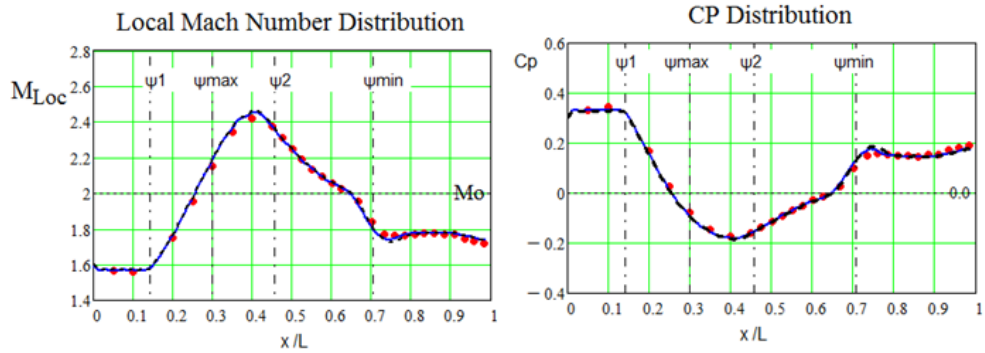


Figure 42: Mach Number and CP Analyses for Mach 2.000, $Re_L = 10.08 \times 10^6$ and $x_t/L = 0.025$

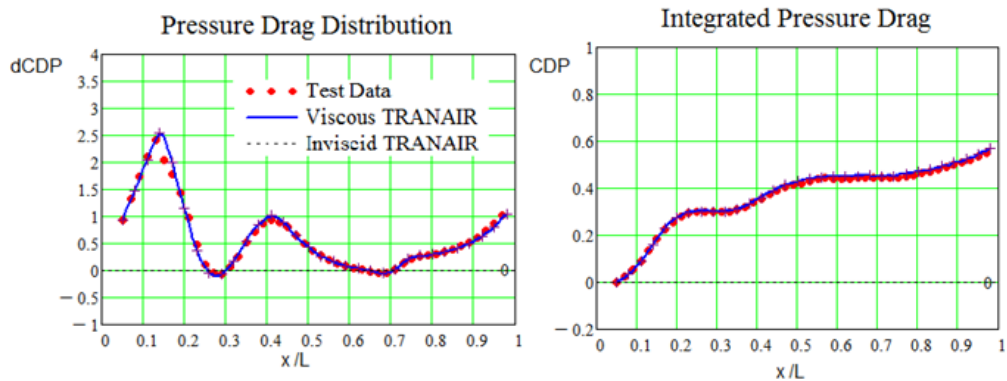


Figure 43: Pressure Drag Analyses for Mach 2.000, $Re_L = 10.08 \times 10^6$ and $x_t/L = 0.025$

The local skin friction predictions are less than experiment in the divergent regions and greater than the experimental data in the convergence region from the maximum area to the minimum area station. The predicted integrated viscous drag however matches the experimental values.

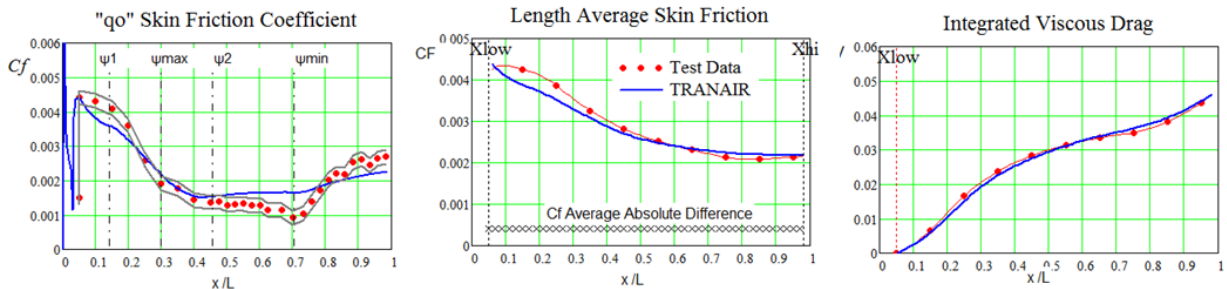


Figure 44: Skin Friction and Viscous Drag Analyses for Mach 2.000, $Re_L = 10.08 \times 10^6$ and $x_t/L = 0.025$

The predicted boundary layer thickness matches the experimental boundary layer thickness. The other boundary layer thickness parameters in figure 45 match the experimental data quite well.

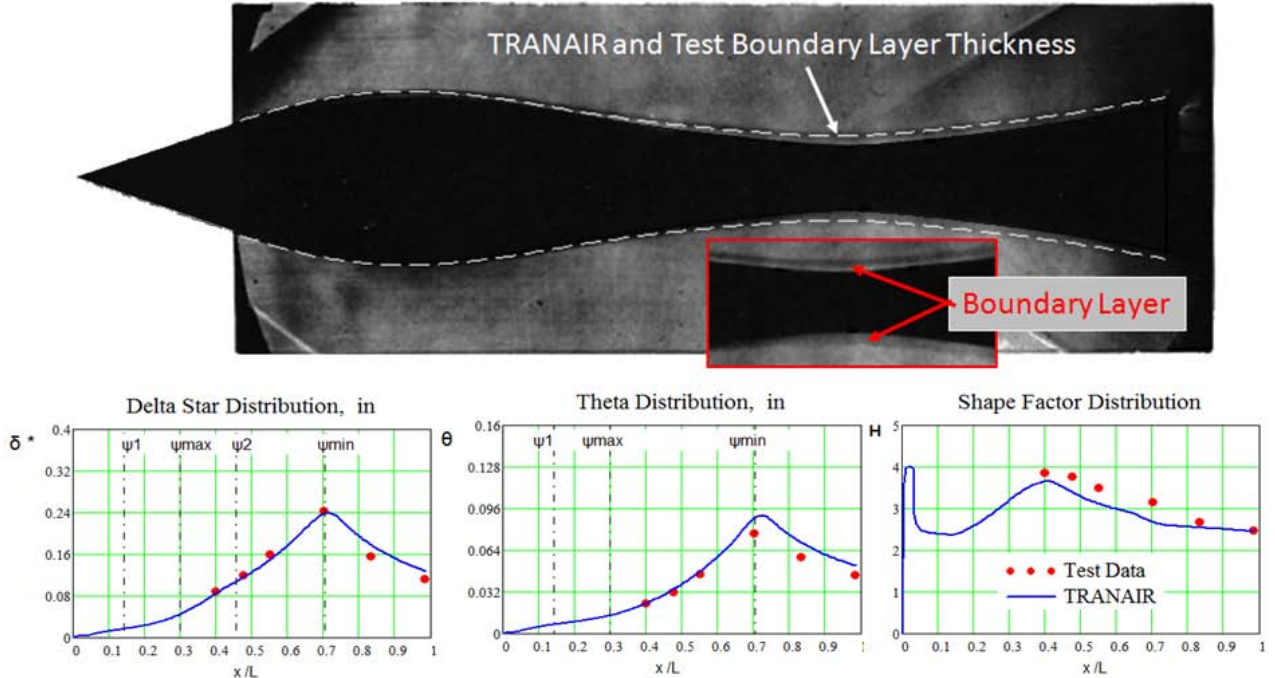


Figure 45: Boundary Layer Analyses for Mach 2.000, $Re_l = 10.08 \times 10^6$ and $x_t/L = 0.025$

Figures 46, 47 and 48 show the results of TRANAIR predictions and the corresponding test data at Mach 2.0 for a Reynolds number of 17×10^6 . The predictions and the test data are quite similar to those previously shown for the Reynolds number of 10^6 .

The theoretical local pressure distribution and local Mach distribution very closely match the test measurements in figure 46.

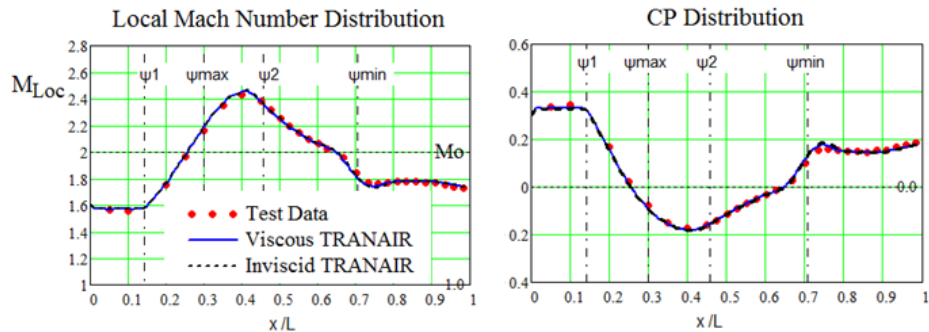


Figure 46: Mach Number and C_p Analyses for Mach 2.002, $Re_l = 16.85 \times 10^6$ and $x_t/L = 0.025$

The theoretical pressure drag distribution and the integrated pressure drag distributions shown in figure 47 are identical with the corresponding wind tunnel measurements

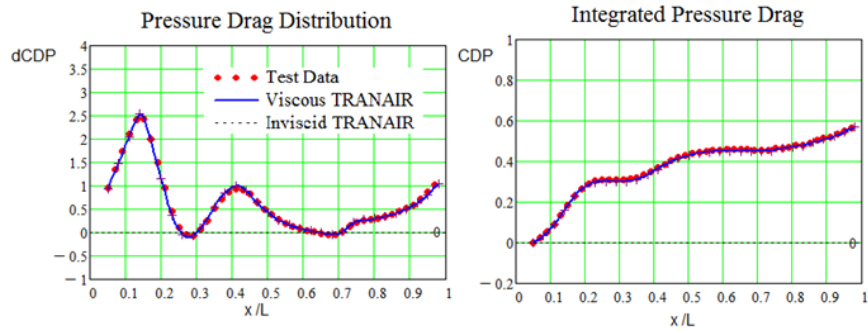


Figure 47: Pressure Drag Analyses for Mach 2.002, Rel = 16.85×10^6 and $x_t/L = 0.025$

The theoretical local skin friction distribution shown in figure 48 is very similar to the test data in the region of the favorable pressure gradient to the 40% body station. Beyond that station the theoretical predictions are higher than the test data in the converging flow region down to the minimum area station and slightly lower than the test data in the diverging flow region on the flared aft body.

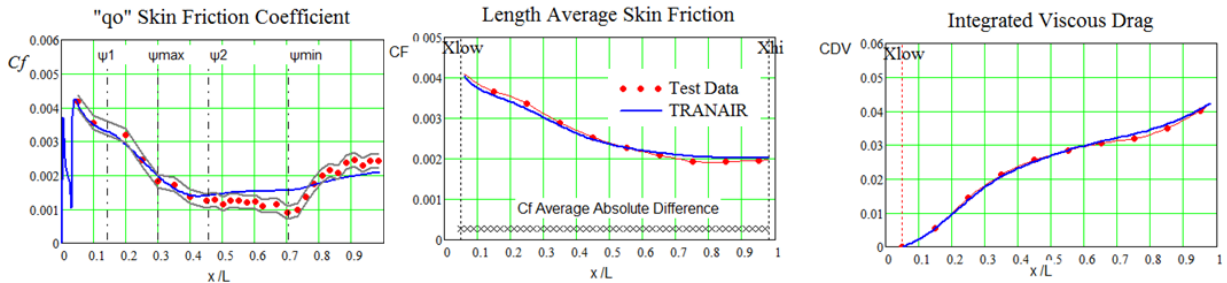


Figure 48: Skin Friction and Viscous Drag Analyses for Mach 2.002, Rel = 16.85×10^6 and $x_t/L = 0.025$

XI. Supersonic Analyses Results for Mach ≈ 2.4

The TRANAIR analyses for a Mach number of 2.4 are compared with test data in figures 49 through 53. The predicted pressure distribution and pressure drag distributions in figure 49 and 50 are close to the experimental data.

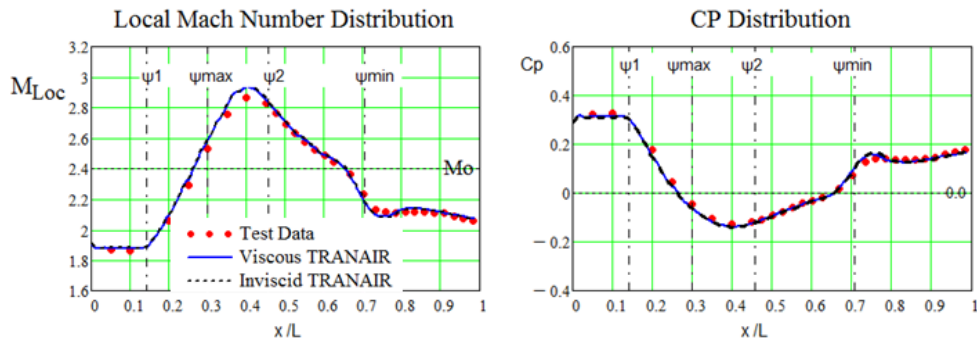


Figure 49: Mach Number and Cp distributions for Mach 2.401, Rel = 10.03×10^6 and $x_t/L = 0.025$

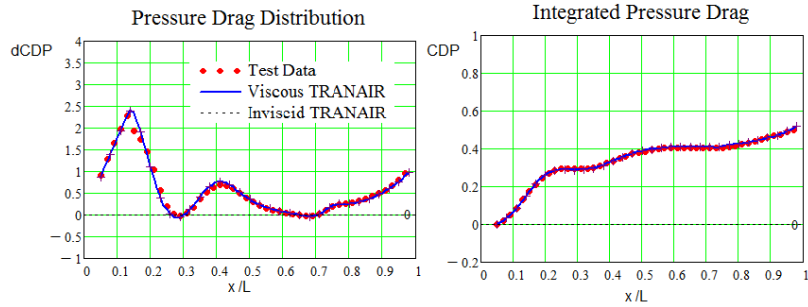


Figure 50: Pressure Drag Analyses for Mach 2.401, $Rel = 10.03 \times 10^6$ and $xt/L = 0.025$

The theoretical local skin friction distribution predictions as in the previous supersonic analyses closely resemble the experimental local skin friction distribution. The theoretical local skin friction values are slightly lower in the diverging flow regions and slightly higher in the converging flow regions. Consequently the overall average skin friction coefficient and the overall viscous drag coefficient equal the corresponding experimental values.

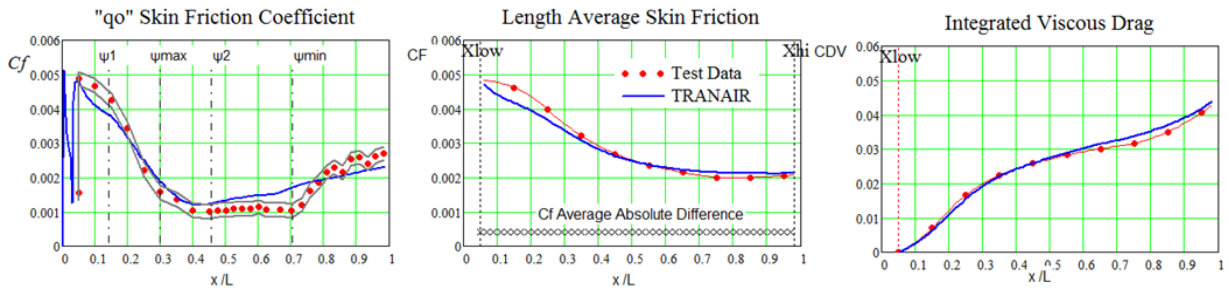


Figure 51: Skin Friction and Viscous Drag Analyses for Mach 2.401, $Rel = 10.03 \times 10^6$ and $xt/L = 0.025$

The predicted boundary layer thickness matches the boundary layer thickness indicated in the schlieren picture in figure 52

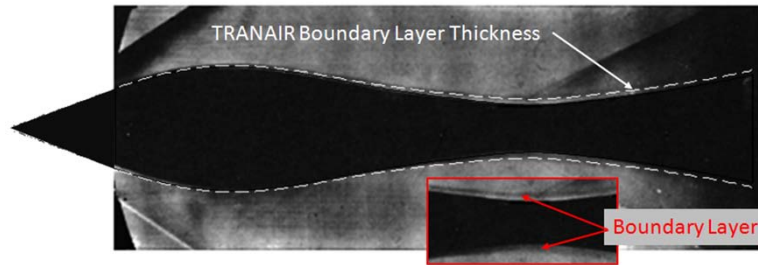


Figure 52: Theoretical and Experimental Boundary Layer Thickness Distributions, Mach 2.401, $Rel = 10.03 \times 10^6$

The theoretical predictions of the displacement thickness distribution and the momentum thickness distribution are significantly larger than the experimental measurements. These differences are rather surprising since the theoretical pressure distribution and local skin friction distribution were both quite close to the test data.

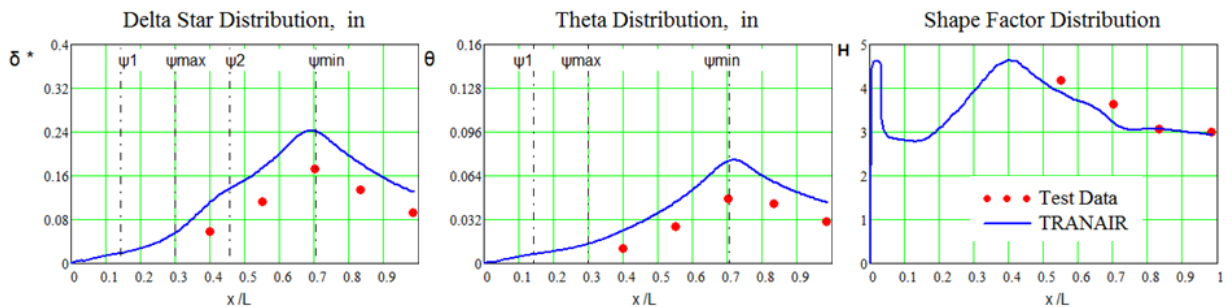


Figure 53: Boundary Layer Analyses for Mach 2.401, $Rel = 10.03 \times 10^6$ and $xt/L = 0.025$

XII. Supersonic Analyses Results for Mach ≈ 2.8

The results obtained at the highest test Mach number of Mach 2.8 at a Reynolds number of approximately 5 million are shown in figures 54 through 56. At this Reynolds number the boundary layer trip was not effective the boundary layer. Consequently, the theoretical data shown in these figures were obtained with a trips free analysis

The theoretical viscous and inviscid predictions of the local Mach numbers are significantly higher than the test data beginning at the maximum area station and into the converging flow region to slightly beyond the end of the favorable pressure gradient region. The theoretical predictions are then close to the test data in the remaining converging flow region down to the minimum area station. The theoretical predictions are then less than the test data on the flared aft body.

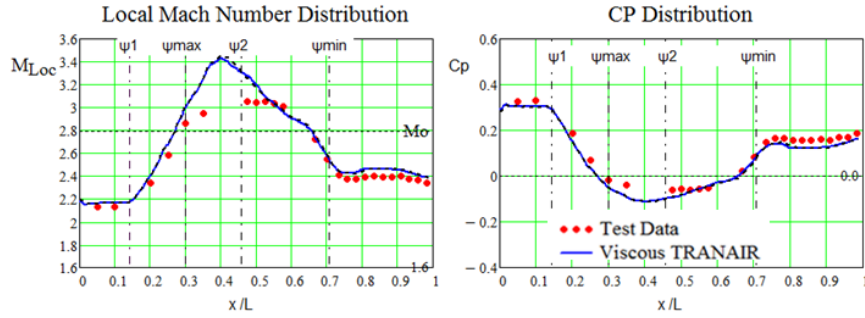


Figure 54: Un-tripped Mach Number and Cp Distributions for Mach 2.793, $Re_l = 5.03 \times 10^6$

The theoretical pressure drag distribution is therefore greater than the test results in the region following the maximum area station back to slightly beyond the favorable pressure gradient region. The theoretical integrated pressure drag distribution however, is overall quite close to the test results. The total theoretical pressure drag is exactly equal to that of the test data. This is a classic example that illustrates the fact that test versus theory comparisons of total force measurements are not sufficient to judge the overall validity of a theoretical methodology.

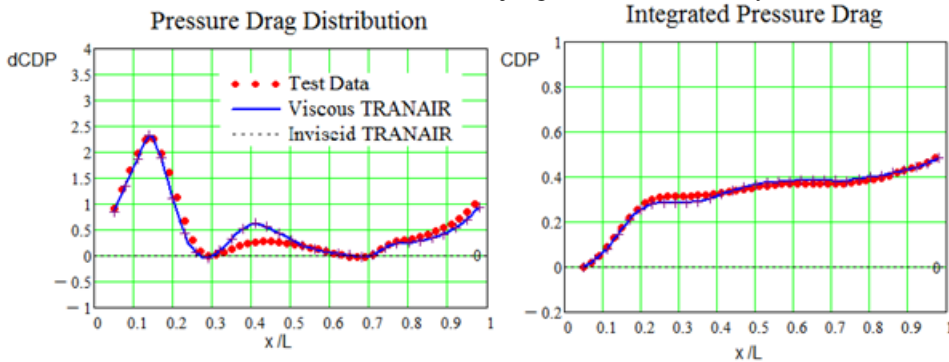


Figure 55: Un-tripped Pressure Drag Distributions for Mach 2.793, $Re_l = 5.03 \times 10^6$

The theoretical trips free analysis predictions of the local skin friction distribution on the WSR body are compared with the test results in figure 56. The theoretical local skin friction predictions are quite close but slightly higher than the test results up to the location the predicted boundary layer transition location, $x_t/L \approx 0.46$. The experimental boundary layer transition process appears to occur over a region slightly beyond the theoretical transition location. The theoretical local skin friction predictions are close to the test data in the diverging flow region on the aft flared body. The predicted average skin friction and viscous drag are greater than the test data primarily because of the skin friction differences in the boundary layer transition region.

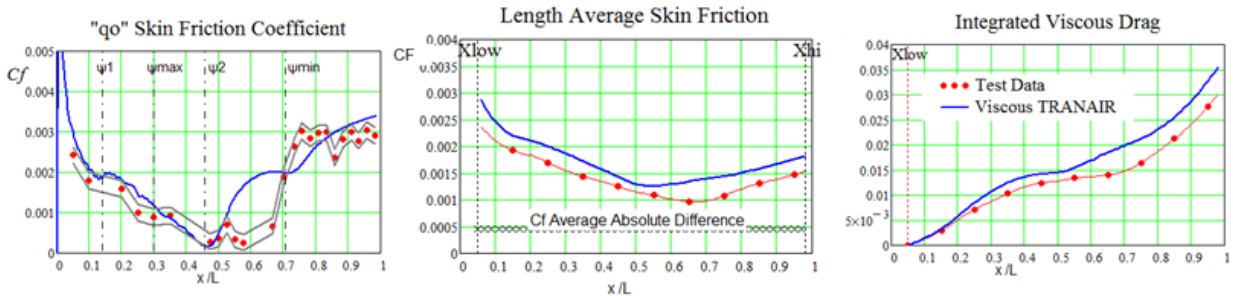


Figure 56: Un-tripped Skin Friction and Viscous Drag Distributions for Mach 2.793, $Re_l = 5.03 \times 10^6$

Figures 57 through 60 show the results obtained for approximately the same Mach number but at a higher Reynolds number where the experimental boundary layer trips were effective in tripping the boundary layer.

The experimental local Mach number distribution is much closer to the theoretical local Mach number distribution than previously shown for the lower Reynolds number results in figure 54. The theoretical local Mach numbers are still somewhat higher than experiment in the region beyond the maximum area station. The differences in the theoretical and the experimental local Mach number distributions shown in figure 54 and 57 are clearly related to a Reynolds number phenomena not captured in the theoretical predictions.

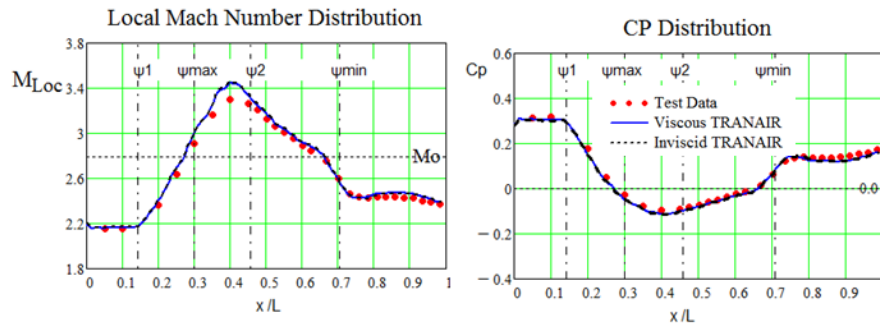


Figure 57: Mach Number and C_p Distributions for Mach 2.799, $Re_l = 10.03 \times 10^6$, $x_t/L = 0.025$

The predicted pressure drag distribution and the integrated pressure drag distributions shown in figure 58, are very close to the test results.

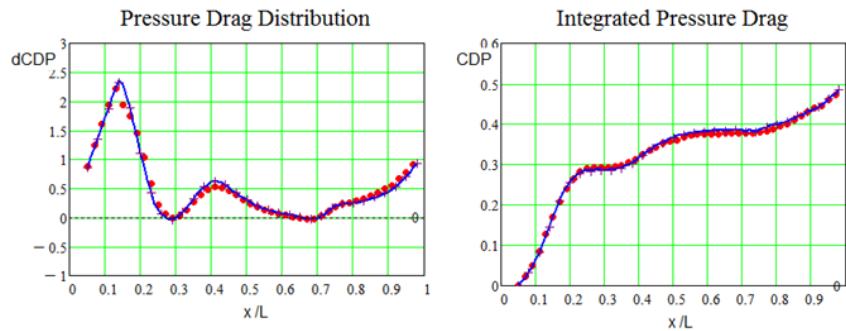


Figure 58: Pressure Drag Distributions for Mach 2.799, $Re_l = 10.03 \times 10^6$, $x_t/L = 0.025$

The theoretical and experimental local skin friction distributions are shown in figure 59. It appears that the experimental transition region actually occurred slightly aft of the theoretical station at 2.5% of the body length, and then developed over the conical forebody. The theoretical skin friction consequently is significantly higher than the experimental results in this region. Over the remainder of the body the theoretical local skin friction distribution is similar to the experimental distribution. The theoretical average skin friction coefficients and the integrated viscous drag are greater than the corresponding test results over the entire body.

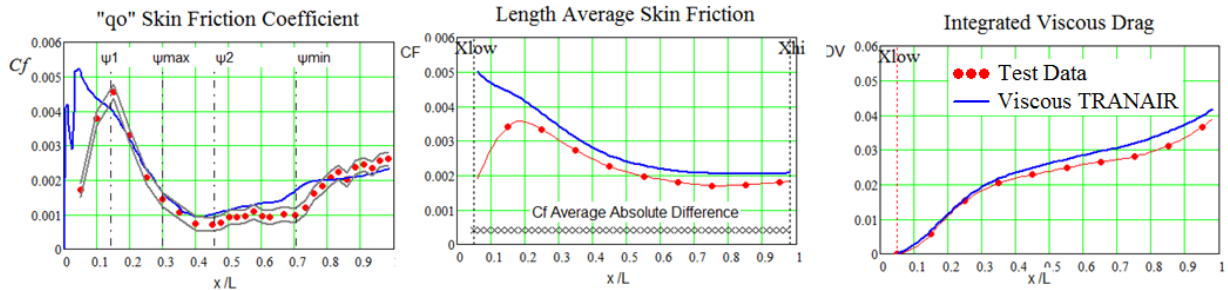


Figure 59: Skin Friction and Viscous Drag Distributions for Mach 2.799, $Rel = 10.03 \times 10^6$, $xt/L = 0.025$

The predicted distributions of the displacement thickness and the momentum thickness are significantly higher than the corresponding test results as shown in figure 60. These results are similar to the Mach = 2.4 results shown in figure 53. These results suggest that there is a high Mach number boundary layer growth phenomenon which is not properly captured by the theoretical methodology.

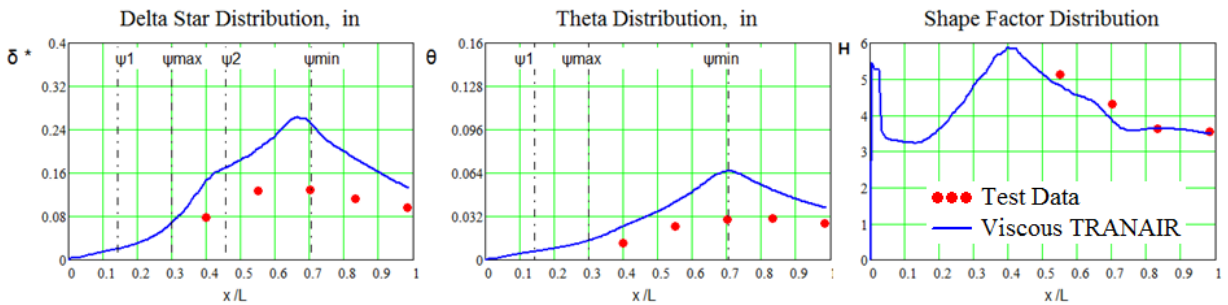


Figure 60: Boundary Layer Parameters Distributions for Mach 2.799, $Rel = 10.03 \times 10^6$, $xt/L = 0.025$

XIII. Summary of TRANAIR and Experimental Data Comparisons

The results of the previously shown test versus theory comparisons are summarized for a Reynolds of 10 million in figures 61, 62 and 63.

The WSR body which was the subject of this investigation as shown in figure 61, was designed to have regions of both divergent and convergent flows. This geometry produced regions of both favorable and unfavorable pressure gradients that are somewhat different for the subsonic and supersonic flow conditions.

The predicted local Mach number distributions shown in figure 61 are in very good agreement with the test data except at the highest Mach numbers of 2.4 and 2.8 (shown in figure 57) where the theoretical predictions are somewhat greater than test over the front of the body in the region back to the end of the favorable pressure gradient region which occurs at approximately 40% of the body length.

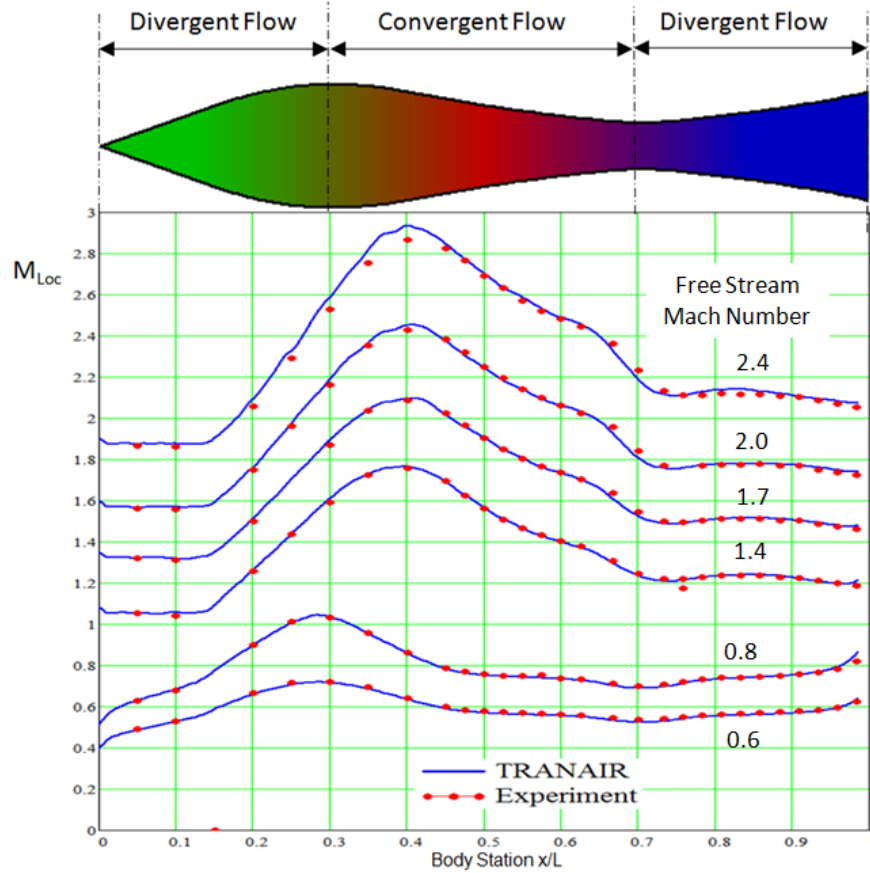


Figure 61: Local Mach Number Distributions

The predicted pressure drag is in excellent agreement with the test results for the entire subsonic through supersonic test regime as shown in figure 62. The predicted viscous drags for the subsonic test conditions are greater than the experimental results. The viscous drag predictions agree very well with the test data for the supersonic test conditions.

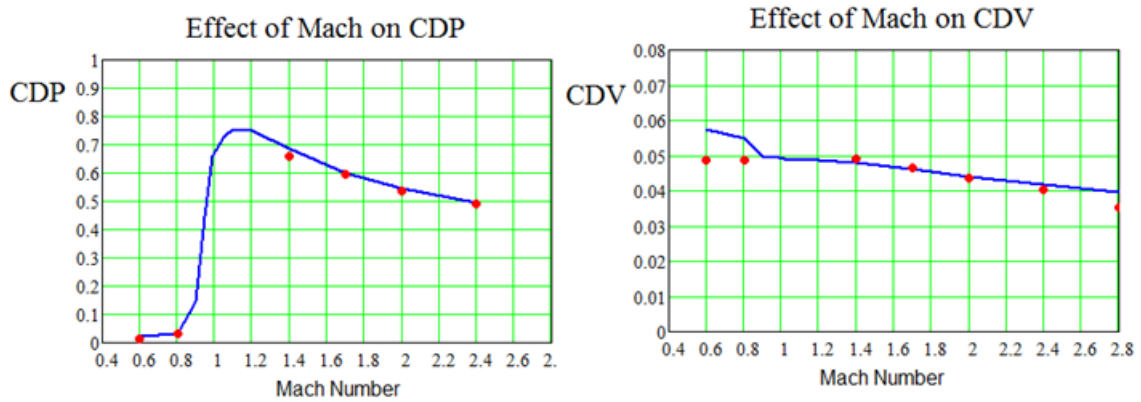


Figure 62: Pressure Drag and Viscous Drag Comparisons

The predicted values of the maximum displacement thickness were generally occurred at the minimum area station are close to the test data except at the highest Mach numbers. The predicted values of the maximum momentum thickness were generally higher than experiment.

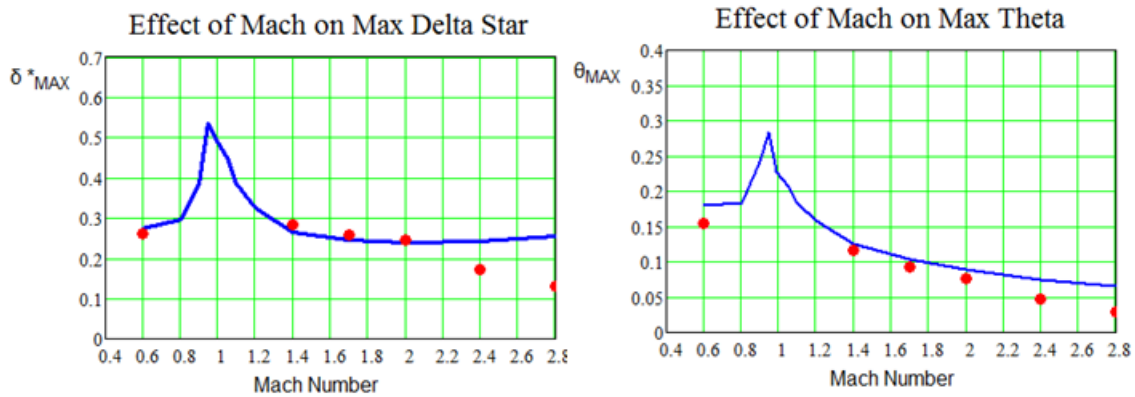


Figure 63: Boundary Layer Growth Parameter Comparisons

An important conclusion of the investigation described in this report is shown by the friction drag results presented in figure 64.

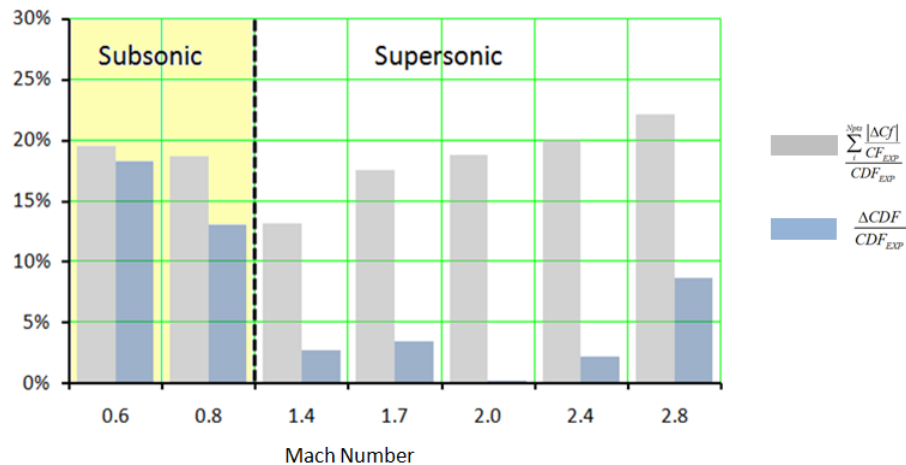


Figure 64: Comparison of Local Skin Friction Prediction Errors and viscous Drag Prediction Errors

This figure presents the viscous drag prediction errors $\frac{\Delta CDF}{CDF_{EXP}}$ and ratios of the average absolute local skin friction errors $\frac{\sum_i^{Npts} |\Delta Cf_i|}{CF_{EXP}}$ to the corresponding experimental average skin friction coefficients at the end of the body for all of the analysis Mach numbers at a Reynolds number of approximately 10 million.

At subsonic Mach numbers the average absolute local skin friction errors are slightly larger than the total force viscous drag errors. However the supersonic results show that the local skin friction errors in the present investigation were much larger than the total viscous drag errors. This clearly shows that good agreements between theoretical total force predictions and corresponding experimental total force measurements are not sufficient to validate the details of a theoretical methodology. A validation process should therefore include detailed fundamental comparisons such as those presented in this study

Acknowledgements

The author would like to acknowledge and give thanks to Robin G. Melvin and Craig L. Hilmes from the Boeing Commercial Airplanes Enabling Technology and Research Organization for their critical contributions in providing the author a specially developed TRANAIR analysis process. This convenient and systematic analysis process enabled the author to conduct the extensive series of TRANAIR analyses described in this report.

References

1. Brenda M. Kulfan, B.M, Bussoletti, J.E. and Hilmes, C.L., "Pressures and Drag Characteristics of Bodies of Revolution at Near Sonic Speeds Including the Effects of Viscosity and Wind Tunnel Walls", AIAA--2007-0684, 45th AIAA Aerospace Sciences Meeting and Exhibit, Jan. 2007
2. Brenda M. Kulfan, B.M, Bussoletti, J.E. and Hilmes, C.L., "Aerodynamic Characteristics of Bodies of Revolution at Near-Sonic Speeds", JOURNAL OF AIRCRAFT., Vol. 44, No. 6, Nov.–Dec. 2007
3. Winter, K.G.(1965), Rotta, J.C. and Smith, K.G., "Untersuchungen der Turbulenten Grenzschicht an einem taillerten Drehkorper bei Unter-und Überschallatromung", Aerodynamische Versuchsanstalt Gottingen AVA-FB 65-09, Sept. 1965
4. Winter, K.G.(1969), Rotta, J.C. and Smith, K.G., "Turbulent Boundary Layer Studies on a "Waisted Body of Revolution in Subsonic and Supersonic Flow", - Translation from German by Neffgen, F. , Office of International Operations.
5. Winter, K.G.(1970), Rotta, J.C. and Smith, K.G., "Studies of the Turbulent Boundary Layer on a Waisted Body of Revolution in Subsonic and Supersonic Flow", Aeronautical Research Council R & M No. 3633, 1970
6. J.N. Hool, "Measurement of skin friction using surface tubes.", Aircraft Engineering 28, 52-54. 1956.
7. K.G. Smith, K.G., Gaudet, L. and Winter, K. G. "The use of surface pitot tubes as skin-friction meters at supersonic speeds", A.R.C.R. & M. 3351. June 1962.
8. East, L. F., "Measurement of Skin Friction at Low Subsonic Speeds by the Razor-Blade Technique", Aeronautical Research Council R. & M. No. 3525, August, 1966
9. Wyatt, L. A. and East, L.F., "Low-speed measurements of skin friction on a slender wing.", A.R.C.R. & M. 3499. February 1966.
10. Bussoletti, J. E., Johnson, F. T., Bieterman, M. B., Melvin, R. G., Young, D. P. and Drela, M., "TRANAIR: Solution Adaptive CFD Modeling for Complex 3D Configurations", in Proceedings of the 1993 European Forum - Recent Developments and Applications in Aeronautical CFD, Royal Aeronautical Society, Sept. 1993, pp. 10.1-10.14.
11. Bieterman, M. B., Bussoletti, J. E., Hilmes, C. L., Johnson, F. T., Melvin, and Young, D.P., "An Adaptive Grid Method for Analysis of 3D Aircraft Configurations", Computer Methods in Applied Mechanics and Engineering, 101 (1992), pp. 225-249.
12. M. Drela, "Two-Dimensional Transonic Aerodynamic Design and Analysis Using The Euler Equations", PhD dissertation, MIT, 1985.
13. M. Drela, "Integral Boundary Layer Formulation for Blunt Trailing Edges". AIAA Paper 89-2200, Aug. 1989
14. Kornilov, V.I., Litvinenko, Y.A. and Pavlov, A.A., "Skin-Friction Measurements in an Incompressible Pressure-Gradients Turbulent Boundary Layer. Review of Techniques and Results.", ADM001433, International Conference on Methods of Aerophysical Research (11th), Novosibirsk, Russia, Jul 2002
15. Preston, J. H., The determination of turbulent skin friction by means of pitot tubes, J. R. Aeronaut. Soc. London, 58, 109–121, 1954.